JOURNAL OF QUATERNARY SCIENCE (2023) **38**(4) 526–543 ISSN 0267-8179. DOI: 10.1002/jqs.3493

JQS Journal of Quaternary Science QRA Quaternary Research Association

The patchwork loess of Central Asia: Implications for interpreting aeolian dynamics and past climate circulation in piedmont regions

ADITI K. DAVE,[1,2]* LENKA LISÁ,[3,4] GIANCARLO SCARDIA,[5] SAIDA NIGMATOVA[6] and KATHRYN E. FITZSIMMONS[1,2]

[1]Research Group for Terrestrial Palaeoclimates, Max Planck Institute for Chemistry, Mainz, Germany
[2]Department of Geosciences, University of Tübingen, Schnarrenbergstrasse 94-96, 72076, Tübingen, Germany
[3]Institute of Geology, Czech Academy of Sciences, Prague, Czech Republic
[4]Nuclear Physics Institute of the Czech Academy of Sciences, CRL Radiocarbon Laboratory, Na Truhlářce 39/64, 18086, Prague 6, Czech Republic
[5]Instituto de Geociências e Ciências Exatas, Universidade Estadual Paulista (UNESP), 13506-900, Rio Claro SP, Brazil
[6]Institute of Geological Sciences K. Satpaeva, Ministry for Education and Science of the Republic of Kazakhstan, Almaty, Kazakhstan

Received 6 May 2022; Revised 9 October 2022; Accepted 27 November 2022

ABSTRACT: Reconstruction of mass accumulation rates (MARs) in loess deposits are widely used for interpreting long-term aeolian transport and climate dynamics in terrestrial environments. However, these interpretations are often driven by a preponderance of reconstructions from individual or selected sites, which can bias our understanding of past climate, especially in the absence of other proxy information. Recent studies on MARs from multiple loess sites in Arid Central Asia (ACA) reveal disparities in the timing of peaks in accumulation between sites, as well as asynchronies with loess flux in the Chinese Loess Plateau (CLP). We investigate this issue by (1) dating five new sites from the western Ili Basin, therefore extending the spatial cover of loess chronologies across ACA and (2) combining that with MARs from >30 sites across ACA and the CLP over the last 60 ka. Our results indicate spatio-temporal inhomogeneity in the timing and rate of loess deposition across the ACA, and highlight the importance of interrogating local and regional influences on dust supply and transport. Our synthesis of MARs from ACA and the CLP suggests that the timing of peak dust flux as an indicator of large-scale climate dynamics is best derived from an aggregate of sites; this removes site-specific bias where local processes or topographic settings outweigh the climate signature. © 2023 The Authors. *Journal of Quaternary Science* Published by John Wiley & Sons Ltd.

KEYWORDS: Central Asia; Chinese Loess Plateau; loess; luminescence dating; mass accumulation rates

INTRODUCTION

Dust is an important constituent of the climate system. It can act as a trigger for climate change, whether directly by altering the radiative balance of the Earth, or indirectly by changing the optical properties of clouds (Arimoto, 2001; Andreae and Rosenfeld, 2008). Iron in mineral dust acts as a limiting nutrient in oceans, increasing ocean productivity and thereby atmospheric greenhouse gas concentrations, thus acting as an additional indirect driver of climate change (Martin, 1990; Martínez-García *et al.*, 2014). Conversely, the production, transport and deposition of dust reflects an earth-surface response to climatic conditions. Consequently, deposits of wind-blown dust, known as loess (Pye, 1987; Pécsi, 1990), are recognised as significant terrestrial archives of past climate change (Liu, 1985; Smalley, 1995; Smalley *et al.*, 2005; Muhs, 2007), especially at semi-arid and subhumid temperate latitudes (Fitzsimmons, 2017).

Reconstruction of changes in loess accumulation rates is one of the most commonly used parameters for inferring past climatic conditions and atmospheric dust load. The quantification of loess sedimentation as mass accumulation rates (MARs) not only facilitates direct comparison between different sites, but also the reconstruction of large-scale dust flux patterns over glacial–interglacial timescales (Kohfeld and Harrison, 2003). In addition, loess MAR datasets provide input for models to better understand the role of dust feedback mechanisms within the climate system (Albani and Mahowald, 2019; Schaffernicht *et al.*, 2020). On this basis, it is essential to ensure that interpretation of MAR datasets reflects a robust understanding of the various geological and climatic factors affecting loess accumulation rates in a given region.

Loess MARs as a gauge for palaeoenvironmental conditions is based on the widespread assumption that loess accumulation increases during drier, colder and/or windier climate phases, and decreases and is overprinted by soil development during wetter, warmer and/or less windy periods. It is this hypothesis on which correlations between loess profiles are overwhelmingly predicated, both within (e.g. Kukla *et al.*, 1988; Kohfeld and Harrison, 2003; Sun and An, 2005; Fitzsimmons *et al.*, 2012) and between regions (Marković *et al.*, 2015). Calculations of loess accumulation are mostly based on luminescence dating, which determines the timing of burial of ubiquitous quartz and feldspar minerals and which, having a higher upper dating limit than radiocarbon, can therefore extend the chronological length of the quantitative record (Singhvi *et al.*, 2001; Stevens, 2019). Recently, an increase in studies applying high-resolution luminescence dating to loess deposits has started to suggest a lack of uniformity in accumulation rates (Újvári *et al.*, 2010; Fitzsimmons *et al.*, 2017), even at individual sites (e.g. Fitzsimmons and Hambach, 2014; Sprafke *et al.*, 2018; Stevens *et al.*, 2018; Fenn *et al.*, 2020). These results call into question the

*Correspondence: Aditi K. Dave, as above.
Email: aditikrishna.dave@gmail.com

presumed primary association between loess accumulation and climatic controls, and prompt a reconsideration of geological controls on aeolian flux.

Central Asia (hereafter 'Arid Central Asia' or ACA), defined here as the region to the north of the Asian high mountains and between the Caspian Sea and Mongolia, is an arid region that lies at the intersection of two major Northern Hemisphere climate systems, the mid-latitude Westerlies and the Siberian High. ACA is assumed to be a major contributor to the global dust cycle (Narisma *et al.*, 2007; Kok *et al.*, 2021), based on both its climatic context and widespread thick loess deposits. The region therefore represents an invaluable natural laboratory for exploring loess accumulation as a response to climate. Recently produced chronological datasets from loess sites in ACA (Li *et al.*, 2016a, 2018a; Fitzsimmons *et al.*, 2018) indicate a high degree of variability in the timing and peak of loess accumulation between sites, therefore challenging prevailing assumptions linking aeolian flux to cold, dry phases and with the timescales of glacial–interglacial climate variability. It has since been suggested, on the basis of modelled dust trajectories, that the topographic complexity and diverse landscape features (desert dunes, stony pavements, alluvial deposits and floodplains) in ACA lead to a complex interaction between topography, wind dynamics, and sediment availability and supply (Fitzsimmons *et al.*, 2020). We therefore expect that it is not just climate that plays a major role in dictating the pattern and distribution of loess flux in this region and possibly elsewhere, but that other factors must be taken into equal consideration.

In this study, we investigate spatial variability in the timing and rates of loess accumulation across the Ili Basin of southeast (SE) Kazakhstan, and in ACA more widely. We undertake a twofold approach. First, we obtain a high-resolution chronological record based on luminescence dating for five loess sites in the as yet understudied central and western part of the Ili Basin; providing an additional 200 km of spatial coverage to the loess record in the region. We integrate our new chronologies with published luminescence-dated loess records from the eastern part of the basin to derive a conceptual understanding of aeolian dynamics within the Ili Basin with respect to timing and topography. Second, we calculate MARs for all reliably dated Ili Basin loess sites, as well as for additional sites across ACA and the Chinese Loess Plateau (CLP), to synthesise the spatial distribution of dust flux and the timing of peak accumulation with respect to geographical setting and larger scale climate drivers across Central and East Asia.

REGIONAL SETTING

ACA is a predominantly arid to semi-arid region, defined here as extending from the Caspian Sea in the west to the Mongolian Hangay uplands in the east (Schaetzl *et al.*, 2018). ACA forms a wide belt in the rain shadow north of the Asian high mountains, including the actively uplifting Pamir, Alai and Tien Shan (Schurr *et al.*, 2014; Grützner *et al.*, 2017). The region features loess-draped piedmonts, alluvial fans, dune fields and the large endorheic basins of the Aral Sea and Lake Balkhash. ACA experiences an extremely continental, semi-arid climate. Its present-day climate is driven by the interaction between two main climatic features — the mid-latitude Westerlies and the high-altitude polar front, linked to the Siberian High Pressure system, from the north. Seasonal variations in wind direction and precipitation are strongly influenced by the interaction between these subsystems and the orography of the region (Lydolph, 1977; Machalett *et al.*, 2008).

This study focuses on the loess deposits that drape the piedmonts of the central and eastern Tien Shan mountain ranges within the Ili Basin, located in SE Kazakhstan and northwest China. The Ili River (also referred to as Yili, Fig. 1) is the main inflow of Lake Balkhash; its main tributaries include the Kashi, Tekes and Kunes rivers, which originate in the upper, Chinese part of the basin. The Ili Basin is surrounded by the Tien Shan mountain ranges to the south, the Chinese Borohoro range to the east, and the Dzhungarian Alatau and northern Tien Shan to the northeast, forming a funnel shape that opens to the west, exposing it to the prevailing westerly and northerly winds and the associated dust transport pathways believed to facilitate loess accumulation along the piedmonts. The basin opens out at the 'Ili Gate' onto the alluvial fans, plains and dunefields of the 'Ili plain' (Fitzsimmons *et al.*, 2020).

The source of loess in the Ili Basin and along the Tien Shan piedmont of the Ili plain is still unclear. Early models (e.g. Obruchev, 1945) posit that the dune fields of the Ili plain to the north, including the Saryesik-Atyrau and Taukum (Fig. 1), act both as sediment sinks for material transported from the Tien Shan, and as sources for dust entrainment and transport back onto the piedmont. Recent investigations based on loess bulk geochemistry and grain size from the eastern, Chinese side of the Ili Basin (Li *et al.*, 2018b) suggest that the loess is predominantly locally sourced, with distal, desert-derived material increasing in contribution westward along the

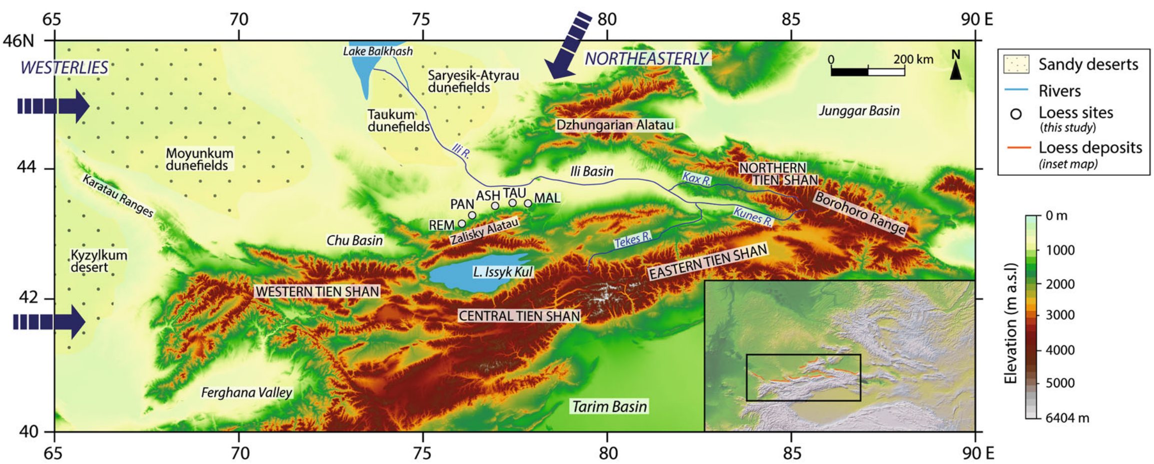

Figure 1. Regional setting and location of the loess sites under study. The elevation map was made using open source Shuttle Radar Topography Mission (SRTM) data provided by AW3D of the Japan Aerospace Agency. [Color figure can be viewed at wileyonlinelibrary.com]

piedmont. Models for fine-grained sediment transport suggest that both local and distal transport, as well as the funnelling or obstructing effect of topography, play a role (Fitzsimmons *et al.*, 2020). The setting of individual sites with respect to topography and sediment transport would therefore likely influence the degree to which loess sediments accumulate and preserve responses to past climatic conditions.

Loess deposits in the Ili catchment vary substantially in thickness, from more than 100 m (Song *et al.*, 2014) to less than 1 m. The distribution and thickness of loess in the eastern (Chinese) part of the Ili Basin was described by Song *et al.* (2014); as yet there is minimal data available for the western and central (Kazakh) part of the basin (Sprafke *et al.*, 2018). Likewise, in the past decade, a number of high-resolution dated loess records have been published from the eastern, Chinese, part of the Ili Basin (ChongYi *et al.*, 2012; Song *et al.*, 2012, 2015; Kang *et al.*, 2015; Li *et al.*, 2018a, 2020; Wang *et al.*, 2019a,b; Yang *et al.*, 2020), while the central, Kazakh part of the basin remains largely unexplored. Field observations along the Kazakh Ili piedmonts in 2015 (Sprafke *et al.*, 2018) and again in 2017 suggest that loess deposits here, in contrast to the Chinese Ili (Song *et al.*, 2014) are discontinuous, highly variable in thickness and are distributed along the mountain foothills, infilling valleys and draping alluvial plains along the range front. Here we investigate five loess sections from a *c.* 200 km east–west (E–W) transect along the Tien Shan piedmont within the Ili catchment, extending from the enclosed part of the basin, through the Ili Gate and onto the Ili plain (Fig. 1).

MATERIAL AND METHODS

Fieldwork and site description

We sampled five loess sections from a *c.* 200 km E–W transect along the Zailisky Alatau range front in SE Kazakhstan (Fig. S1). Since all sites were exposed as vertical cliff sections, we undertook fieldwork by abseil to ensure continuous down-profile observations and sampling. Prior to sampling, we cleared back at least 50 cm of the surface sediment to prevent contamination by recent sediment relocation and expose undisturbed sections. A brief description of our site locations is given below.

Remizovka (hereafter REM, 43° 13.2′ N, 76° 51′ E; 1070 m a.s.l.) is a >25 m thick section exposed on a hillslope, originally excavated for the construction of ski jump facilities on the southern margins of Almaty city. Loess at the site has previously been described and dated by luminescence (Machalett *et al.*, 2006, 2008; Fitzsimmons *et al.*, 2018; Sprafke *et al.*, 2018). A radiocarbon-dated subsection, which has since been removed during road construction (referred to as Tramplin, Feng *et al.*, 2011), was recently placed in stratigraphic context to clarify ambiguity between studies (Sprafke *et al.*, 2018). Our study here focusses on the uppermost 7 m of the main section.

Panfilov (PAN, 43° 22.295′ N, 77° 07.670′ E; 710 m a.s.l.) is a *c.* 5 m thick site located just southwest of the village of Panfilovo, c. 40 km northeast of Almaty. The loess section has been exposed as a result of erosion by the Tsyganski Creek, which flows northward from the Tien Shan.

Ashubulak (ASH, 43° 28.671′ N, 77° 47.379′ E; 760 m a.s.l.) is located at the southern edge of the village of the same name, *c.* 50 km east of the PAN section. The exposed outcrop at this site is 5.1 m thick and is entirely composed of pale yellowish primary loess. Like PAN, the ASH site is also located along the peripheral edge of the piedmont loess, where the loess deposits taper out northwards onto alluvial fans.

Taukaraturyk (TAU, 43° 29.445′ N, 78° 01.509′ E; 769 m a.s.l.) is a 7.5 m thick profile located on the southern edge of the village of Taukaraturyuk, *c.* 20 km and *c.* 100 km east of ASH and Almaty, respectively. Unlike the loess-marginal sites of PAN and ASH, which are located in more open, exposed sections *c.* 10 km out from the range front, the TAU site is located much closer to the mountain ranges (*c.* 1 km north of the first ridge of the Zailisky Alatau).

Malubai (MAL, 43° 26.312′ N, 78° 19.763′ E; 815 m a.s.l.) is located *c.* 20 km south of the city of Chilik (Shelek) and *c.* 25 km east of TAU. The exposed outcrop at MAL is 6 m thick and lies on the northern slope of a northeast–southwest bifurcating flank of the Zailisky Alatau, and is consequently more sheltered than the other sites.

Proxy indices

Samples for micromorphology, grain-size analyses and magnetic susceptibility were collected from four sites (PAN, ASH, TAU and MAL) at 10 cm intervals. We collected these samples in 8 cm^3 plastic boxes hammered into the cleaned-back profiles. The same sample material was used for all three analyses in the order described below. Grain size and magnetic susceptibility data for the site of REM was already available from previous work (Fitzsimmons *et al.*, 2018; Schulte *et al.*, 2018).

Magnetic susceptibility

Magnetic susceptibility measurements were performed on 228 samples from four sites (PAN, ASH, TAU, MAL) using AGICO Kappabridge MFK2 at the Alpine Palaeomagnetism Laboratory (Peveragno, Italy). The samples were air dried at 50°C and measured at room temperature with an alternating current magnetic field with an amplitude of 20 A/m at 976 Hz (low frequency). The low-frequency measurements were repeated two times for each sample; the mean was taken for the final calculation of normalised mass-specific bulk magnetic susceptibility (χ_m).

Micromorphology

Eighteen selected samples were prepared for micromorphological analysis from three loess localities (PAN, ASH and TAU). The samples were impregnated in vacuum chamber using Polylite 2000 and after curing, the thin sections were observed using a polarising microscope at resolution ranges of 16–800× at the Institute of Geology, Czech Academy of Sciences (Prague). The micromorphological descriptions follow Stoops (2003) and are summarised in Table S1 of the supplementary information (SI).

Grain size

Grain-size analyses were undertaken on 228 samples from four sites (PAN, ASH, TAU and MAL) following two different preparation methods: the total dispersion method (Konert and Vandenberghe, 1997) and dispersion in KOH (Łomotowski *et al.*, 2008). For the total dispersion method, samples were dispersed in 10% KOH solution after pre-treatment with HCl and H_2O_2 to remove carbonates and organic matter, respectively. The KOH dispersion method involved measurement following sediment dispersion in 10% KOH solution. All grain-size measurements were undertaken at the Institute of Geology at the Czech Academy of Sciences, Prague, using a CILAS 1190 LD laser particle analyser, with a measurement range of 0.04–2000 μm and analytical error of <2%. We evaluated the mean grain size using the GRADISTAT program (Blott and Pye, 2001). Sedimentology and wind-strength interpretations were made on the basis of mean grain size, the proportion of ≤4 μm grains (determined using both preparation methods), as well as the grain size index (GSI: %26–52 μm/%<26 μm; Antoine *et al.*, 2009; based on the total dispersion method).

Luminescence dating

Samples for luminescence dating were collected at 1 m intervals from all five profiles (REM, PAN, ASH, TAU and MAL) by hammering 3.5 cm diameter, 10 cm long steel tubes into freshly cleaned loess sections. A total of 27 samples were collected from five sites. Additional sediment for dose rate analysis was collected from the material immediately surrounding the tubes. The exposed outer material from the ends of the steel tubes was used for determining water content; sediment from the inner parts of the tubes was processed for equivalent dose analysis. All samples were processed under subdued red-light conditions at the Institute of Geosciences, Johannes Gutenberg University, and measured at the Max Planck Institute for Chemistry, respectively (Mainz, Germany). Wet-sieving of sediment yielded insufficient coarse grains (>63 μm) for measurement; we therefore prepared fine-grained (4–11 μm) quartz and polymineral samples using established protocols (Frechen *et al.*, 1996; Timar *et al.*, 2010).

We measured the equivalent dose (D_e) using optically stimulated luminescence (OSL) based on the single aliquot regenerative dose (SAR) protocol (Murray and Wintle, 2000, 2003) for the quartz fraction, and elevated temperature post-infrared infrared stimulated luminescence (pIRIR; Thiel *et al.*, 2011) for the polymineral fine-grained (K-feldspar-bearing) material. In order to negate the suspicion of any feldspar contamination of the OSL signal from the quartz-rich fine grains, we applied the double-SAR approach (DSAR, Banerjee *et al.*, 2001; Jain and Singhvi, 2001; Dave *et al.*, 2019), which includes an additional IR stimulation prior to all blue stimulation steps within the SAR protocol. In samples where saturation of the quartz OSL signal was suspected (after Timar-Gabor *et al.*, 2017), elevated pIRIR signals from fine-grained polymineral samples was used for D_e determination.

Radionuclide concentrations for dose rate determination were analysed using high-resolution germanium gamma spectrometry, measured at the Felsenkeller, VKTA Dresden. Dose rates were calculated from the radionuclide concentrations using published conversion factors (Guérin *et al.,* 2011), combined with measured moisture content and published equations for cosmic-ray dose rate contributions (Prescott and Hutton, 1994). A detailed account of sample preparation, luminescence measurements and protocols, and dose rate calculations can be found in the SI.

Age–depth modelling and mass accumulation rates

Based on our investigations of fine-grained quartz as discussed below and the reliability of quartz-based OSL ages, we limited our assessment of loess MARs to the past 60 ka. The presence of a substantial number of dated loess sites within this age range allows for a good representation of loess sedimentation patterns across the Ili Basin, elsewhere in ACA and across the CLP.

We undertook age–depth modelling and calculated sediment accumulation rates for 30 additional sites based on published luminescence ages (based on quartz OSL and feldspar pIRIR ages) that span the time period 0–60 ka. Our analysis was based on high-resolution luminescence ages taken from 14 sites across the Ili Basin (including sites from the present study), eight sites from neighbouring sedimentary basins in ACA, and 11 representative sites from the CLP. Age–depth modelling for all sites was performed using the R package Bacon (Blaauw and Christen, 2011). The age–depth models derived using R-Bacon were used to estimate the corresponding sedimentation rates (SR, cm ka^{-1}), and then to evaluate MARs (g $cm^{-2}ka^{-1}$) using the equation: MAR = SR × ρ_{dry} × f_{eol}, where ρ_{dry} is the dry bulk density (g cm^{-3}) and f_{eol} refers to the sediment fraction that is aeolian in nature (Kohfeld and Harrison, 2000). We used a value of f_{eol} = 1 for all calculations, since we assume that loess is entirely aeolian in nature. Based on published literature, we utilised mean bulk density values of 1.5 g cm^{-3} for ACA (based on values obtained by Jia *et al.*, 2018; Wang *et al.*, 2019a; Li *et al.*, 2019a) and 1.48 g cm^{-3} for sites in the CLP (Kohfeld and Harrison, 2003; Kang *et al.*, 2015). Details of the sites analysed in this study (and the selection thereof), criteria for the selection of luminescence ages, age–depth model parameters for R-Bacon, the constraints for MAR calculations and subsequent interpretation of different sites (where relevant) are described in the SI.

RESULTS

Stratigraphy and sediment characteristics

The stratigraphy of our five investigated sections, including grain size and magnetic susceptibility can be seen in Fig. 2. A detailed account of the micromorphological characteristics are summarised in Table S1 of the SI.

We focused on the uppermost 7.0 m of the REM loess profile, which spans *c.* 35–15 ka (based on $pIRIR_{290}$ dating; Fitzsimmons *et al.*, 2018). The top 0.8 m of this section is characterised by recent soil formation, including penetration by living plant roots. A carbonate-enriched subhorizon is observed at 0.8–1.5 m depth, below which massive, homogeneous primary loess is observed down to 7.2 m. The magnetic susceptibility record shows relatively little variation down the profile below the recent soil. The grain-size record similarly yields minimal variations, with the exception of a slight increase in the coarser fraction at 3.9–4.3 m and 5.9–6.1 m depths (Schulte *et al.*, 2018). Additional observations relating to colour indices and pedology are described in Fitzsimmons *et al.* (2018).

The PAN section is 5.1 m thick and overlies a >3.0 m thick fluvial gravel bed; the imbrication of cobbles indicates northward flow. The uppermost 0.5 m of the section comprises modern soil, penetrated by present-day roots. At 0.5–0.7 m, we observe a slightly darker humic horizon, which is intercalated with colluvial loess-like material. Below this layer and down to 0.9 m, colluvial angular clasts (2–4 mm) are observed which grade downwards into loess-like sediment. The upper *c.* 1.2 m yields higher magnetic susceptibility values (*c.* 130–90 × 10^{-8} m^3kg^{-1}) that support our observations of weathering and soil formation. From *c.* 0.9–5.1 m, the section is composed of pale yellowish primary loess, with a carbonate-enriched layer at 0.9–1.2 m. Reduced magnetic susceptibility values (*c.* 60 × 10^{-8} m^3kg^{-1}) below *c.* 1.2 m are consistent with unweathered, primary loess deposits. Micromorphological analyses of four samples (Table S1) from the uppermost primary loess (0.9–2 m depth) shows dominant well-sorted, fine-grained aeolian silt mixed with coarser, angular colluvial material (<4 mm); these observations are supported by the grain-size results (Fig. 2). The total dispersion method, which dissociates aggregates, yields a higher proportion of very fine

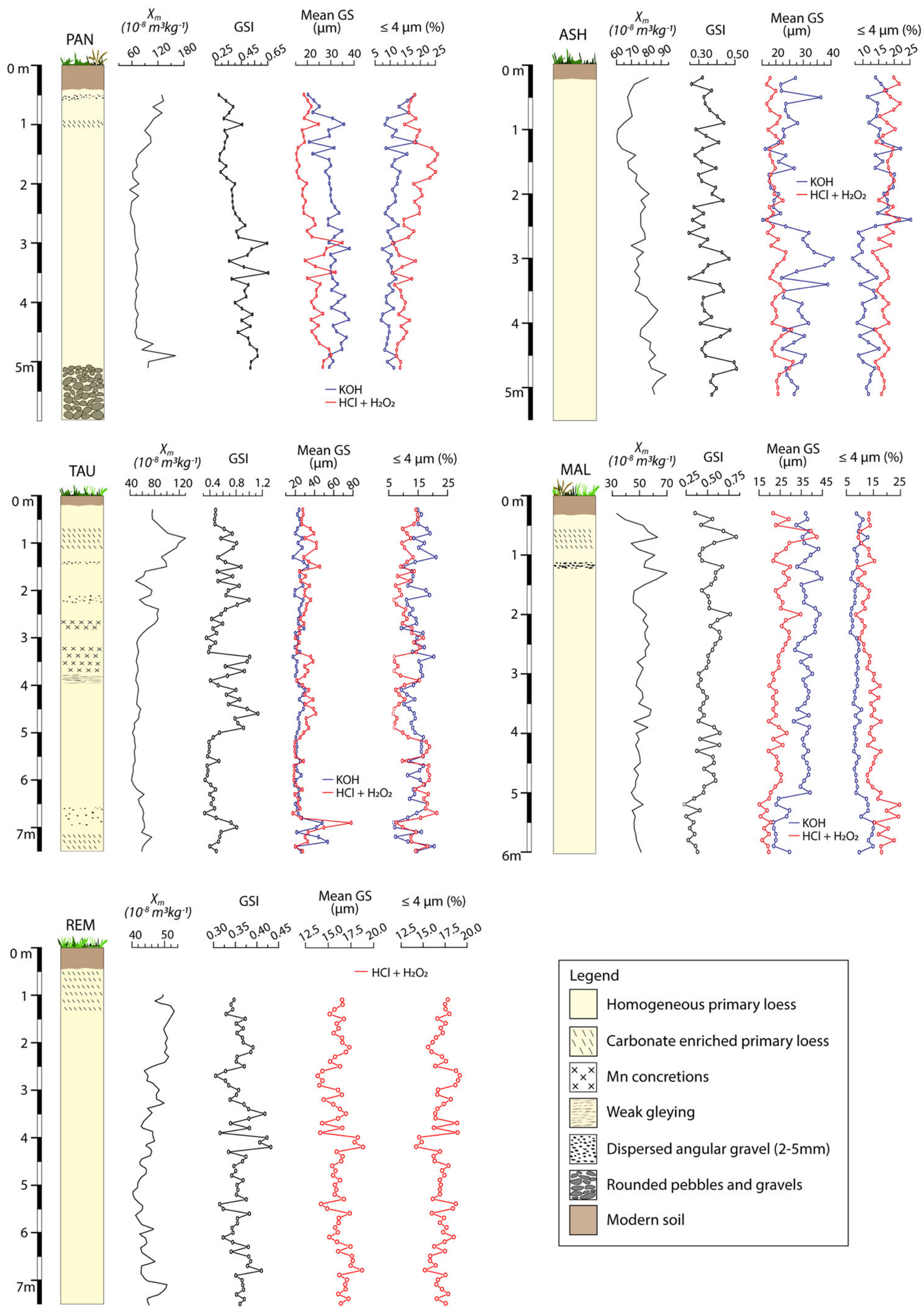

Figure 2. Stratigraphy of the loess sites under study, with down-profile variation in mean grain size (GS), grain size index (GSI) and magnetic susceptibility at the respective sites. The grain size dataset for REM was obtained from Schulte *et al.* (2018) and the magnetic susceptibility at REM is from Fitzsimmons *et al.* (2018). [Color figure can be viewed at wileyonlinelibrary.com]

clasts (<4 μm) than the KOH method, which indicates a high proportion of aggregates from 0.5 to 2.0 m. The aggregates are most likely derived from a combination of colluvial clasts, disintegration of carbonate-coated or carbonate-rich clasts, and aggregation by organic matter present in the sediment. We observe an abrupt increase in magnetic susceptibility at the base of the loess just above the gravels, although the reason for this is unclear.

The outcrop at ASH is 5.1 m thick and is entirely composed of pale yellowish primary loess. The modern soil is *c.* 30 cm thick with modern rootlets. While the geographic situation of ASH is similar to PAN, located along the northern margin of the piedmont loess deposits, the ASH sediments are more consistent with homogeneous, fine-grained primary loess and no colluvial input was observed. Magnetic susceptibility yields no major variations down the profile, which is consistent with primary loess deposition with no evidence of pedogenesis. Micromorphology of five selected samples (Table S1) provides further evidence of minimal disturbance of the sediments following aeolian deposition.

The TAU section is *c.* 7.5 m thick. The uppermost 0.3 m is composed of humic soil with modern rootlets and bioturbation, below which a blocky, carbonate-rich C horizon extends down to 0.7 m. From 0.7 to 7.5 m depth, the section comprises pale yellowish primary loess, with local occurrences of very coarse sand at depths of 1.5–2.0 m, 2.4–2.8 m and 3.8–4.9 m. Carbonate mottling was observed at 1.8–2.9 m and 5.5–7.1 m, and minor manganese concretions occur at 2.4–2.8 m and 3.0–3.8 m. The magnetic susceptibility values show subtle variations along the profile. Higher values (*c.* 90–120 × 10^{-8}

m^3kg^{-1}) occur in the uppermost 2.5 m. We interpret these peaks as incipient pedogenesis which was not observed in the field. There is considerable variation in the GSI in the upper 2.5 m, as well as three distinct increases in mean grain size and the GSI at 3.4–3.8 m, 4.0–5.0 m and 6.0–7.5 m (Fig. 2) which occur as subangular very coarse sand (Table S1). We interpret these peaks as evidence of colluvial input from the nearby bedrock outcrops, which are *c.* 0.7 km south of the site. Micromorphological analysis on six selected samples throughout the profile also identified persistent occurrence of angular gypsum crystals below 1.6 m depth (Table S1), which should represent *in situ* precipitation under arid conditions.

The exposed outcrop of MAL is 6.0 m thick. The uppermost *c.* 0.4 m is composed of modern soil with roots developed within colluvial loess-like material. At 0.4–0.9 m depth, we observe fewer angular clasts within a loess matrix. A discontinuous very coarse sand to gravel layer with silt matrix was observed at 1.1–1.3 m, below which carbonate-rich loess dominates down to *c.* 2 m. Below 2.0 m depth, the section is composed of pale yellowish-beige primary loess, with occasional carbonate mottling and Fe–Mn concretions observed at 2.5–5.0 m. The MAL section yields higher magnetic susceptibility (*c.* 70×10^{-8} m^3kg^{-1}) in the upper 1.5 m, most likely reflecting recent pedogenesis. Mean grain size and GSI vary substantially at 0.5–2.5 m; below 5.0 m, a sudden decrease in grain size is observed. The grain-size variations in the upper 2.5 m most likely reflect variable colluvial input to the silt-dominated aeolian component. Below 2.5 m, the mean grain size, as well as GSI, does not show significant variation and is likely to reflect purely aeolian input to the site. The abrupt decrease of GSI in the primary loess below 5 m most likely indicates a decrease in wind strength (Fig. 2).

Chronology of the Zailisky Alatau loess sections, Central Tien Shan piedmont

The samples in this study were dated using quartz OSL and polymineral pIRIR dating and a detailed record of the luminescence characteristics, equivalent dose and dose-rate estimations and age calculations can be found in the SI. The final age estimates from all five loess profiles in this study are summarised in Table 1 and Fig. 3. Fine-grained quartz OSL ages were derived for 19 samples from four sites (REM, PAN, ASH and the upper 1 m of TAU; Fig. 3) The upper 7 m of the profile REM spans 10–40 ka and falls within the uncertainties of previously published pIRIR ages (Fitzsimmons *et al.*, 2018), while profiles PAN, ASH and the upper 1 m of TAU date to between *c.* 5 and 17 ka. Polymineral fine-grain pIRIR dating on eight selected samples from below 1.5 m at TAU and the entire section at MAL yielded minimum age estimates (Table S2), as these samples exhibited saturation of the $pIRIR_{290}$ signal. Hence, we consider that the deposition below 1 m at TAU and at MAL occurred >180 ka.

Age–depth modelling and mass accumulation rates

Figure 4 shows the location of our sites, as well as of published sites from ACA and the CLP, for which we calculated MARs from luminescence-based chronologies (quartz OSL and feldspar pIRIR ages). We limited our calculations of MARs to the last 60 ka since (i) our investigations suggest an upper limit to reliable dating of quartz in this region (based on saturation of the quartz OSL signal) of *c.* 70 ka, and (ii) most published loess sites in ACA and the CLP span this time period, therefore allowing for a representative evaluation of loess depositional dynamics across these regions.

The MARs of sites in the Ili Basin, elsewhere in ACA and across the CLP are illustrated with respect to concentrations of dust within the Greenland NGRIP ice core (Ruth *et al.*, 2007), stable oxygen isotope records from NGRIP (Rasmussen *et al.*, 2014) and the global marine stack (Lisiecki and Raymo, 2005), and June solar insolation at 65°N (Berger and Loutre, 1991) in Fig. 5. We observe substantial differences in absolute accumulation as well as the timing of peaks in accumulation between sites in the Ili Basin and across ACA more widely (Fig. 5a, b). There are similar differences across the CLP (Fig. 5c). Furthermore, based on our calculations of MARs from 11 sites across the CLP, we observe a distinct difference between sites located in the northwest (NW) and those in the southeast (SE). The geographical difference in loess accumulation in the CLP has previously been reported for various time periods (Lu and Sun, 2000; Kohfeld and Harrison, 2003; Xu *et al.*, 2018; Liu *et al.*, 2020).

DISCUSSION

Spatio-temporal variation in loess deposition along the Central Tien Shan (Zailisky Alatau region)

Our new dataset adds chronological constraints for five loess sites (including new data from REM) from the virtually unexplored Zailisky Alatau piedmont in the western portion of the Ili Basin. Our sites bridge the geographical gap between the relatively intensely studied eastern Ili Basin (ChongYi *et al.*, 2012; Kang *et al.*, 2015; Song *et al.*, 2012, 2015; Li *et al.*, 2016b, 2018a; Wang *et al.*, 2019a,b; Li *et al.*, 2020) and several dated sites further west at Maibulak (MBK) along the Zailisky Alatau (Fitzsimmons *et al.*, 2017), Bishkek (BSK) in the Chu River valley (Youn *et al.*, 2014) and Valikhanova (VAL) on the eastern slopes of the Karatau Range (Fitzsimmons *et al.*, 2017) (Fig. 4a).

We identified phases of loess accumulation and illustrated these with respect to altitude, deposit thickness and distance from the range front in a schematic diagram in Fig. 6. Geographically, the four sites of MBK, REM, PAN and ASH lie west of the Ili Gate and in the more open part of the basin. TAU and MAL lie at approximately the narrowest part of the basin (the 'Gate') and are comparatively sheltered from northerly winds. The sites of PAN, ASH, TAU and MAL lie at similar elevations (*c.* 700-800 m a.s.l.); both MBK and REM are situated at higher altitudes (1070 m a.s.l). The distances of the sites from the range front are also variable. MBK in the west overlies an alluvial fan *c.* 350 m from the range front and *c.* 2 km northward of a steeper break in slope. REM is situated atop a spur of the foothills which rises *c.* 200 vertical metres above the plain, and *c.* 5 km from the major break in slope representing the transition to bedrock ranges. PAN and ASH lie the greatest distance from the range front, *c.* 7.5–8 km to its north. TAU is located *c.* 1 km northward of the first ridge of the Zailisky Alatau, and MAL lies *c.* 150 m north of a bedrock spur and *c.* 2.3 km north of the main range. With the exception of REM, where the range front is oriented approximately SSW–NNE, all sites are situated northward of an east–west trending break in slope. We hypothesise that (1) location within the basin, (2) distance from the range front and (3) its strike are all likely to have played a role in the potential of individual sites to trap aeolian sediment through time.

The westernmost sites, MBK and REM, range in age between 12 and 45 ka (this study; Fitzsimmons *et al.*, 2017, 2018). Although the loess at REM extends downward toward older ages (Machalett *et al.*, 2006; Sprafke *et al.*, 2018), the lack of high-resolution dating >45 ka prevents our consideration of

Table 1. Equivalent dose, dose rate data and luminescence age estimates for fine-grained quartz from the Ili Basin study sites. The term n_e/n_t refers to the total number of accepted discs to the total number of discs measured.

Site	Sample No.	Depth (m)	Moisture attenuated dose rate (Gy/ka)			Cosmic (Gy/ka)	Total dose rate (Gy/ka)	n_e/n_t	De (Gy)	Age (ka)
			Alpha	Beta	Gamma					
Remizovka (REM)	L-EVA-1475	1.1 ± 0.10	0.5 ± 0.1	2.0 ± 0.2	1.2 ± 0.1	0.20 ± 0.02	3.8 ± 0.4	24/24	48.2 ± 0.5	12.8 ± 1.2
	L-EVA-1476	2.1 ± 0.10	0.5 ± 0.1	2.3 ± 0.2	1.3 ± 0.1	0.17 ± 0.02	4.3 ± 0.4	24/24	75.7 ± 1.0	17.8 ± 1.6
	L-EVA-1477	3.1 ± 0.10	0.6 ± 0.1	2.3 ± 0.2	1.4 ± 0.1	0.15 ± 0.02	4.4 ± 0.4	22/24	86.0 ± 1.2	19.7 ± 1.9
	L-EVA-1478	4.1 ± 0.10	0.5 ± 0.1	2.2 ± 0.2	1.3 ± 0.1	0.13 ± 0.01	4.1 ± 0.4	24/24	88.4 ± 1.4	21.7 ± 2.0
	L-EVA-1479	5.1 ± 0.10	0.5 ± 0.1	2.2 ± 0.2	1.2 ± 0.1	0.12 ± 0.01	4.0 ± 0.4	24/24	99.1 ± 1.6	24.9 ± 2.3
	L-EVA-1480	6.1 ± 0.10	0.5 ± 0.1	2.2 ± 0.2	1.2 ± 0.1	0.11 ± 0.01	4.0 ± 0.4	24/24	107.0 ± 2.0	26.5 ± 2.5
	L-EVA-1481	7.1 ± 0.10	0.5 ± 0.1	2.2 ± 0.2	1.3 ± 0.1	0.10 ± 0.01	4.0 ± 0.4	24/24	127.0 ± 2.0	31.5 ± 2.9
Panfilov (PAN)	A0017	1.0 ± 0.05	0.5 ± 0.1	2.2 ± 0.2	1.3 ± 0.1	0.21 ± 0.02	4.2 ± 0.2	19/19	23.1 ± 0.3	5.5 ± 0.3
	A0019	2.0 ± 0.05	0.4 ± 0.1	1.9 ± 0.2	1.1 ± 0.1	0.18 ± 0.02	3.6 ± 0.2	19/19	38.5 ± 0.5	10.6 ± 0.7
	A0021	3.0 ± 0.05	0.5 ± 0.1	2.1 ± 0.2	1.2 ± 0.1	0.16 ± 0.02	3.9 ± 0.2	16/17	47.4 ± 1.8	12.0 ± 1.1
	A0023	4.0 ± 0.05	0.5 ± 0.1	2.0 ± 0.2	1.2 ± 0.1	0.14 ± 0.01	3.9 ± 0.2	20/20	63.4 ± 1.6	16.4 ± 1.3
	A0025	5.0 ± 0.05	0.5 ± 0.1	2.2 ± 0.2	1.3 ± 0.1	0.13 ± 0.01	4.0 ± 0.2	16/17	64.4 ± 2.6	15.9 ± 1.4
Ashubulaq (ASH)	A0026	0.5 ± 0.05	0.4 ± 0.1	1.8 ± 0.2	1.1 ± 0.1	0.24 ± 0.02	3.6 ± 0.2	20/20	45.9 ± 0.6	12.9 ± 0.9
	A0028	1.5 ± 0.05	0.5 ± 0.1	2.1 ± 0.2	1.3 ± 0.1	0.20 ± 0.02	4.1 ± 0.2	20/21	52.6 ± 2.0	12.7 ± 1.1
	A0030	2.5 ± 0.05	0.5 ± 0.1	2.2 ± 0.2	1.3 ± 0.1	0.17 ± 0.02	4.2 ± 0.2	19/20	51.1 ± 2.0	12.3 ± 1.1
	A0032	3.5 ± 0.05	0.5 ± 0.1	2.3 ± 0.2	1.3 ± 0.1	0.15 ± 0.02	4.2 ± 0.2	20/20	63.0 ± 1.3	14.9 ± 1.0
	A0034	4.5 ± 0.05	0.5 ± 0.1	2.2 ± 0.2	1.3 ± 0.1	0.14 ± 0.01	4.1 ± 0.2	21/22	63.5 ± 1.1	15.6 ± 1.1
Taukaraturyuk (TAU)	A001	0.5 ± 0.05	0.4 ± 0.0	1.8 ± 0.1	1.1 ± 0.1	0.24 ± 0.02	3.5 ± 0.2	22/22	46.6 ± 1.4	13.3 ± 1.0
	A002	1.0 ± 0.05	0.5 ± 0.1	2.0 ± 0.2	1.2 ± 0.1	0.21 ± 0.02	3.9 ± 0.2	22/22	44.9 ± 0.7	11.4 ± 0.8
	_A003*_	_1.5 ± 0.05_	_0.5 ± 0.1_	_2.0 ± 0.1_	_1.2 ± 0.1_	_0.19 ± 0.02_	_3.9 ± 0.2_	_8/8_	_305.1 ± 13.8_	_78.3 ± 7.1_
	_A0016*_	_7.5 ± 0.05_	_0.5 ± 0.1_	_2.3 ± 0.2_	_1.3 ± 0.1_	_0.10 ± 0.01_	_4.2 ± 0.2_	_7/11_	_301.6 ± 22.4_	_71.5 ± 8.5_
Malubai (MAL)	_A0037_[i]	_1.0 ± 0.05_	_0.6 ± 0.1_	_2.0 ± 0.2_	_1.2 ± 0.1_	_0.21 ± 0.02_	_4.0 ± 0.2_	_3/3_	_339.7 ± 17.0_	_84.9 ± 8.5_
	_A0037*_	_1.0 ± 0.05_	_0.8 ± 0.1_	_2.4 ± 0.2_	_1.6 ± 0.1_	_0.20 ± 0.02_	_5.0 ± 0.2_	_3/3_	_339.7 ± 17.0_	_67.9 ± 6.1_
	_A0050*_	_5.1 ± 0.05_	_0.7 ± 0.1_	_2.5 ± 0.2_	_1.6 ± 0.1_	_0.13 ± 0.01_	_4.9 ± 0.2_	_3/3_	_373.1 ± 18.5_	_76.1 ± 6.8_

[i]A0037 has unusually low uranium content compared with the samples from the rest of the profile. Hence, the age derived here maybe overestimated due to low dose rate and so we use the dose rate of A0038.
*The text shown in Italics are saturated ages from quartz estimated from dose–response curves constructed at high doses.

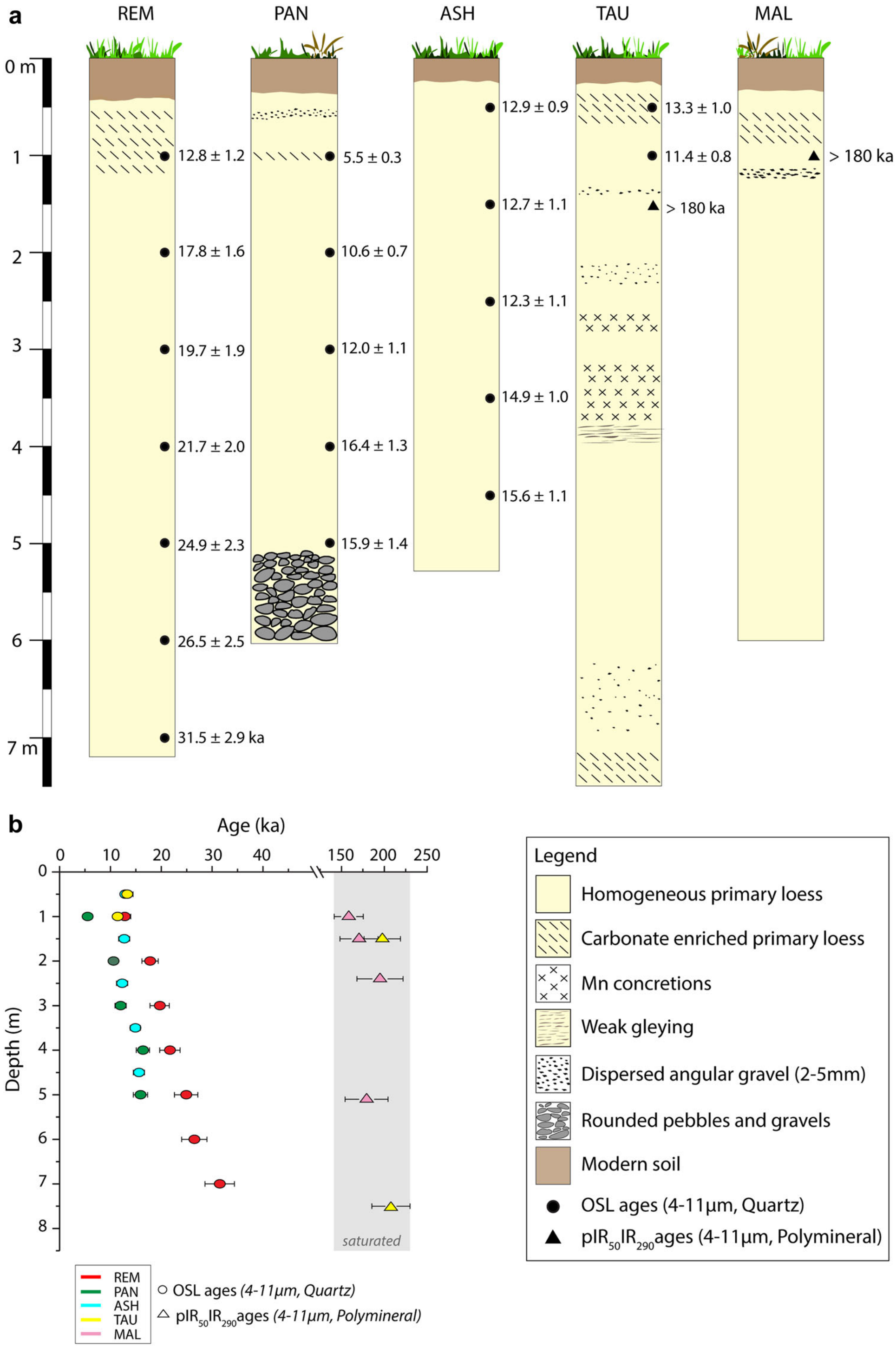

Figure 3. (a) Stratigraphy of all the sites with the luminescence ages obtained in this study. (b) Plot of optical ages (2σ uncertainty) as a function of depth for all sites. [Color figure can be viewed at wileyonlinelibrary.com]

accumulation during earlier periods. By contrast, the two central sites, PAN and ASH, are substantially younger in age and span much shorter periods of time; 17–5 ka and 15–12 ka, respectively. The site of TAU, situated *c.* 20 km east of ASH, preserves *c.* 1 m of loess accumulation during a similar time period to ASH (*c.* 11–13 ka) and overlies an unconformity with substantial hiatus, below which the loess exceeds 180 ka. The easternmost Zailisky Alatau site of MAL predates 180 ka and yielded no late Pleistocene deposits. We hypothesise that the location of TAU and MAL within the more sheltered Ili Gate area led to reduced loess accumulation over the late Pleistocene compared with the more exposed western sites. Increased wind strength related to a 'funnelling' effect by the enclosing mountain ranges may also have led to the erosional unconformities observed at TAU and MAL.

While loess grain size is often used as a proxy for wind intensity through time (An *et al.*, 1991a; Porter and An, 1995; Sun and An, 2005; Vandenberghe, 2013), our observations from the Ili Basin loess deposits strongly suggest that additional controls, such as geomorphic setting, sediment availability and supply to individual sites, also influence aeolian flux and grain size. We compared changes in GSI from three study sites (REM, PAN and ASH) with those from the published site of NLK in the eastern part of the basin (Li *et al.*, 2018c), focusing on the time period *c.* 12–16 ka (Fig. 7). GSI values during this interval range from 0.30–0.40 at REM, 0.40–0.65 at PAN,

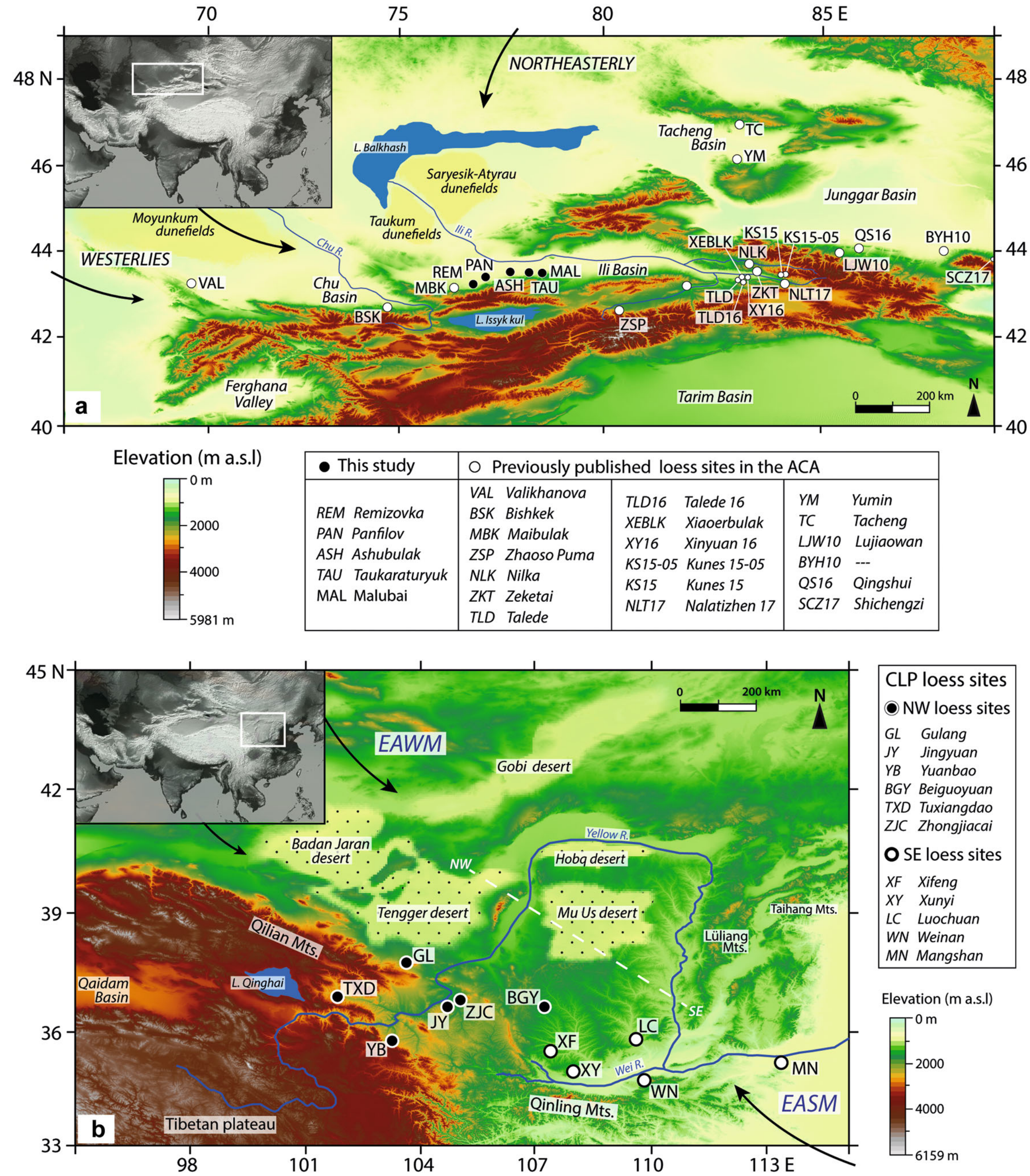

Figure 4. Location and regional settings of all reliably dated loess sites in (a) Arid Central Asia (ACA) and (b) the Chinese Loess Plateau (CLP), for which we calculated mass accumulation rates (MARs). References of all the published loess sites are listed in Table S5 of the SI. The elevation maps in both cases were created using open source SRTM data provided by AW3D of the Japan Aerospace Agency. [Color figure can be viewed at wileyonlinelibrary.com]

0.25–0.45 at ASH, and 0.30–0.60 at NLK. We observe that not only the magnitude of variability in GSI but also the mean value differs between sites. Sediments at PAN are coarser than at ASH, despite the relative proximity of these two sites. GSI values are less variable at REM in the west than at NLK in the east (Fig. 7). These differences within the same time interval along the piedmont suggest spatial variability in sediment supply, transport to and deposition at an individual site. For example, the proximity of both NLK and PAN to active fluvial channels may account for relatively greater amounts of proximal transport of coarser grains (Li *et al.*, 2018c) than can be transported to the other sites. While the site REM, located away from fluvial channels and at a higher elevation relative to the other sites, shows overall finer GSI values and a smaller range of GSI at the site, which may reflect a greater reliance on distal transport and sorting.

The geomorphic context of individual sites is likely to influence not only grain size characteristics and variability through time, but also aeolian flux, expressed here as MARs (Fig. 7). For the 12–16 ka time period, aeolian flux at ASH far exceeds that at any other site, with PAN experiencing the next highest rate of accumulation. We suggest that its relatively low elevation, distance from alluvial fans and range front, and a strengthened westerly trajectory of dust-laden winds at the Ili Gate resulted in higher accumulation here than at any other site along the piedmont for which we have data. On the other hand, while MARs at PAN are lower than at nearby ASH, its GSI range is higher and may reflect greater immixing of proximal fluvial material with distal accumulation. This observation raises questions regarding hitherto popular correlation of proxies such as grain size and aeolian flux

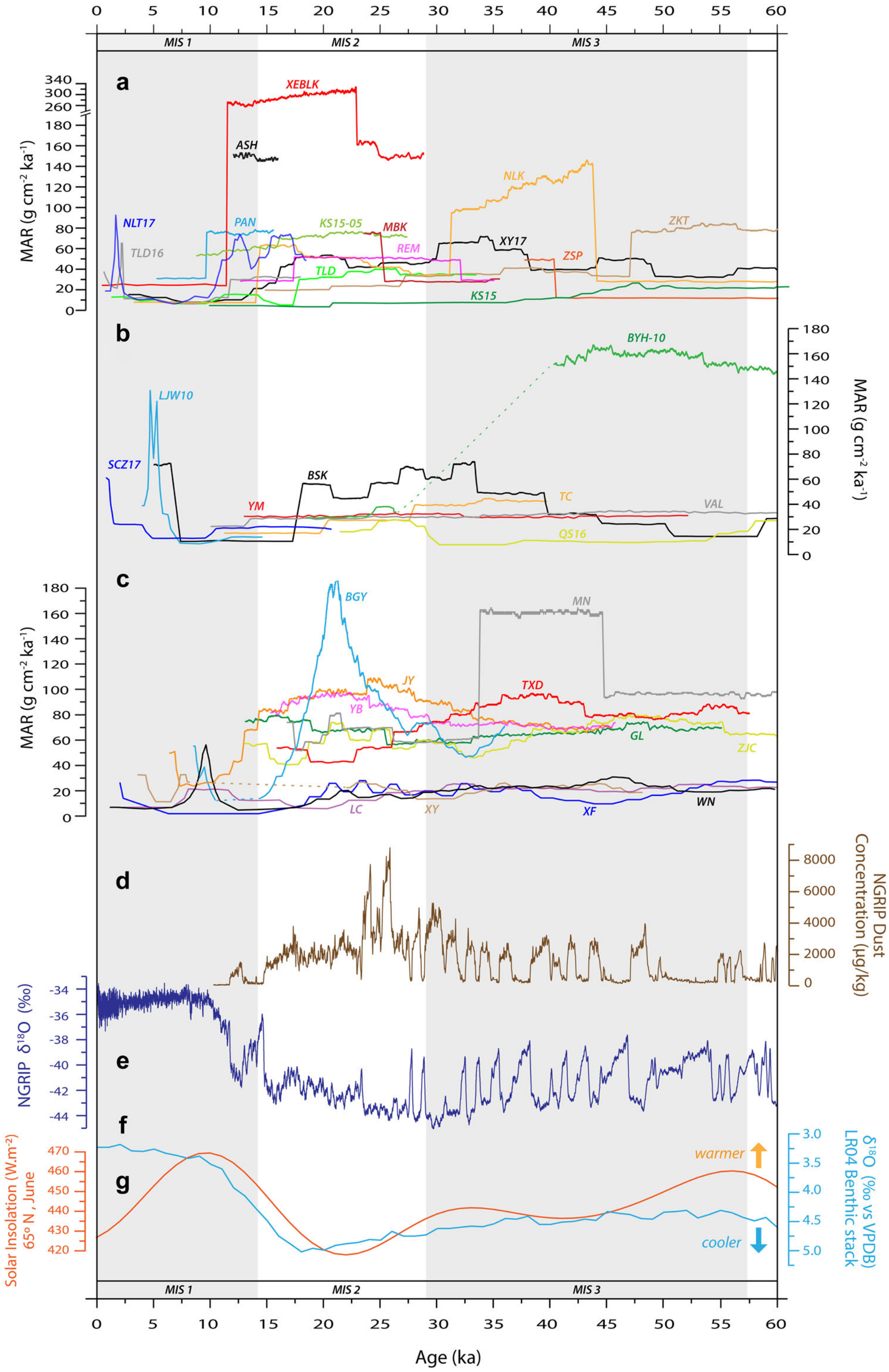

Figure 5. Comparison of mass accumulation rates (MARs) over the past 60 ky for loess sites in (a) the Ili Basin (b) other enclosed basins in Arid Central Asia (ACA) and (c) the Chinese Loess Plateau (CLP). Note the uniform *y*-axis, with the exception of extremely high MARs at XEBLK in the Ili Basin. We compare the loess accumulation rates with (d) NGRIP dust flux (Ruth *et al.*, 2007), (e) NGRIP $\delta^{18}O$ (Rasmussen *et al.*, 2014), (f) stacked benthic foraminifera $\delta^{18}O$ marine record LR04 (Lisiecki and Raymo, 2005) and (g) June insolation at 65°N (Berger and Loutre, 1991). The dashed lines in the MARs represents a depositional unconformity/hiatus at the respective site. [Color figure can be viewed at wileyonlinelibrary.com]

with wind strength in loess deposits generally. The older deposits at MAL and TAU yield GSIs in the 0.4–0.9 range, which is greater than those observed at the other sites. This may relate to the proximity of TAU and MAL to a seismically active range front (Chilik fault), which can introduce coarser clasts to the loess via slope transport. These observations highlight the need to first interrogate the geomorphic setting of individual sites for their potential to reflect local or larger scale processes according to proposed research questions.

We observe along the Zailisky Alatau transect, a 'patchwork' loess piedmont of spatially variable timing of peaks in deposition, flux and grain size. This most likely reflects the result of complex interactions between local and continental wind regimes and associated dust transport, topographic (including palaeotopographic) context, and local sediment supply.

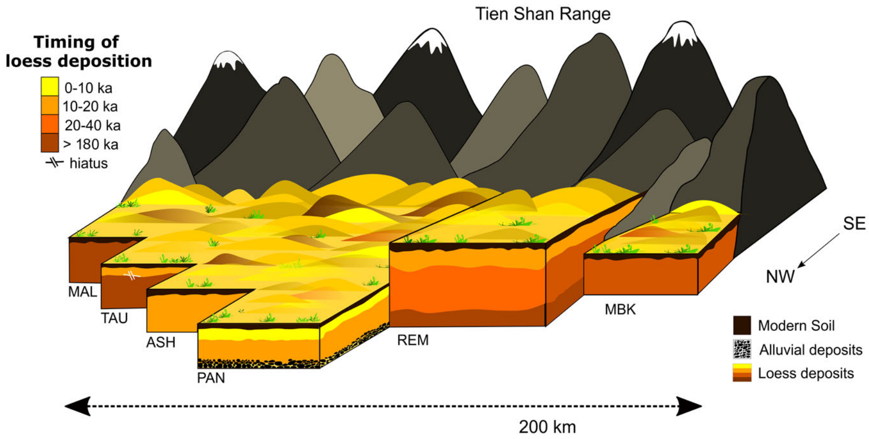

Figure 6. Schematic 3D representation of the timing of loess accumulation phases along the Zailisky Alatau range in the Central Tien Shan, southeast Kazakhstan. [Color figure can be viewed at wileyonlinelibrary.com]

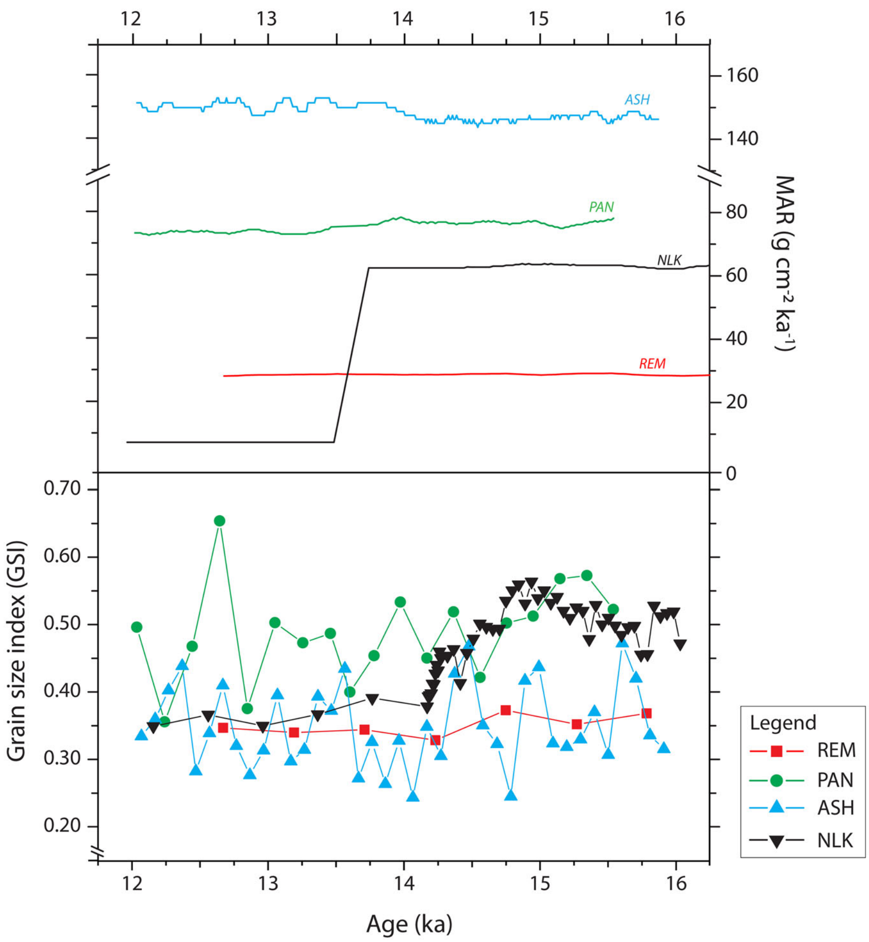

Figure 7. Comparison of mass accumulation rates (MARs) and grain size index (GSI) for late MIS 2 (12–16 ka) from four loess sites (REM, PAN, ASH and NLK) from an east–west transect along the Ili Basin, southeast Kazakhstan. The GSIs for NLK were calculated from published data (Li *et al.*, 2018c). [Color figure can be viewed at wileyonlinelibrary.com]

Loess sedimentation dynamics across the Ili Basin: Overcoming individual site bias to reconstruct the interplay between the Westerlies and the Siberian High Pressure system

The ACA piedmonts, especially the Ili Basin, lie at a pivotal topographic point which exposes the region both to the mid-latitude westerly winds and the Siberian High Pressure, the latter manifesting here in the form of northerly winds associated with the seasonal migration of the high-altitude polar jet (Fitzsimmons *et al.*, 2020). The Westerlies rarely penetrate eastward of the Tien Shan range; loess deposited in this part of ACA therefore represents a strategic record of aeolian transport and deposition associated with both climate subsystems. Published correlations from the eastern Ili Basin loess linking grain size with penetration of westerly air flow suggest that the influence of the Westerlies was neither consistent nor strong over the Late Pleistocene (Li *et al.*, 2018c). The loess deposits of the Ili Gate/Zailisky Alatau region investigated in this study, coupled with data from the eastern Ili Basin, can provide more meaningful information relating to the interplay between the Westerlies and Siberian High climate systems through time.

Here we examine the degree to which loess profiles across the entire Ili Basin record past environmental conditions in the form of accumulation rates. In Fig. 5a, we show MARs from our new datasets from REM, PAN and ASH, in addition to those from 11 published sites (ChongYi *et al.*, 2012; Kang *et al.*, 2015; Song *et al.*, 2012, 2015; Li *et al.*, 2016b, 2018a, 2020; Fitzsimmons *et al.*, 2017, 2018;

Wang *et al.*, 2019a,b), presenting a 60 ka record from the eastern headwaters of the Basin to the 'Ili Gate'.

We observe substantial differences in absolute MARs between sites, not only over the 60 ka range but also over shorter timescales such as the deglacial and marine isotope stage (MIS) 3 interstadials. We hypothesise that absolute MARs are likely to reflect differences in topographic settings between individual sites. Absolute sedimentation rates at NLK, for example, are approximately five times higher than those observed at the sites KS15 and XY17 during late MIS 3 (40–27 ka). NLK is located on the banks of the Kax River (Kashi; Song *et al.*, 2015), whereas KS15 is located in the easternmost Ili Basin and on the upper terraces of the Kunes River (Li *et al.*, 2018a). While both these rivers, tributaries of the Ili, derive from glacial sources, the closer proximity of NLK to the river banks implies a higher sediment availability during MIS 3, when glaciers in the Tien Shan expanded in response to increased moisture transport to ACA (Koppes *et al.*, 2008). The topographic setting of KS15 is also likely to have resulted in relatively low aeolian flux during other time periods. The site KS15-05 (Wang *et al.*, 2019a), located *c.* 3 km east of KS15 (Figs. 4a and 5a), yielded MARs three times higher than at KS15 during late MIS 2 and early MIS 1 and is likely to relate to the closer proximity of the former to the active river channel.

There is also considerable variability in the timing of peaks in loess accumulation across the basin. For example, despite the proximity of the two eastern Ili Basin sites NLK and ZKT (Fig. 4a and Fig. 5a), the former yields peak MARs during late MIS 3 (*c.* 45–30 ka) and the latter peaks during early MIS 3 (*c.* 60–47 ka). These site-specific variations in loess sedimentation rates raise questions regarding how representative the MARs of individual sites may be for understanding regional climatic variations. We propose instead that aggregated trends in loess MARs from multiple sites across a basin are more likely to reflect changes in climate dynamics, thus providing the best means to overcome the bias of individual sites based on their local setting.

We observe a general increase in sedimentation across the entire Ili Basin during interstadial MIS 3 (29–57 ka; Lisiecki and Raymo, 2005); this builds on findings from previous studies which noted primary loess accumulation at this time in the Zailisky Alatau area (Fitzsimmons *et al.*, 2018). Fitzsimmons *et al.* (2018) hypothesised that increased loess flux during late MIS 3 (*c.* 40–27 ka) was due to a general increase in sediment availability and wind strength at this time. Increased sediment supply was likely to be linked to glacial advances in northern and eastern Tien Shan (Kong *et al.*, 2009; Li *et al.*, 2011, 2014; Chen *et al.*, 2015) driven by increased moisture transport by the Westerlies, which is also responsible for the weak pedogenesis observed within the loess during this time (Song *et al.*, 2012, 2015; Fitzsimmons *et al.*, 2018). Furthermore, it has been proposed that the Siberian High, which intensified during late MIS 3 (Ding *et al.*, 1995; Hao *et al.*, 2012), would have compressed the Westerlies against the Tien Shan ranges and increased wind strength into the Ili valley (Fitzsimmons *et al.*, 2018). The combination of increased sediment availability and wind strength in the Ili Basin would therefore have contributed to increased loess accumulation observed in aggregate during this period (Fig. 5a). Local katabatic winds might also have played an important role during this phase, resulting in localised effects on the timing and peaks of loess sedimentation.

We also observe generally increased accumulation rates in aggregate during MIS 2 (29–14 ka, Lisiecki and Raymo, 2005) (Fig. 5a). These conditions coincide with globally cold climates prevailing during the Last Glacial Maximum (26–19 ka LGM; Clark *et al.*, 2009). In the Ili Basin the conditions were not only cooler, but also more arid: stable carbon isotopic ($\delta_{13}C_{org}$) reconstructions for palaeovegetation in the valley indicate an increase in more arid-adapted C_4 vegetation (Ran and Feng, 2013). A cold, dry, windy climate appears to have resulted in coarser grain sizes within a number of loess sequences across the Ili Basin (Song *et al.*, 2015; Li *et al.*, 2016b, 2018c). Climate simulation models indicate windier LGM conditions, due either to stronger mid-latitude Westerlies (Sun *et al.*, 2012) or intensified Siberian high pressure (Cheng *et al.*, 2021). Glacial expansion during MIS 2 in the Central and Eastern Tien Shan (Kong *et al.*, 2009; Li *et al.*, 2011, 2014; Lifton *et al.*, 2014; Blomdin *et al.*, 2016), also resulted in increased production of silt, therefore according availability within the Ili catchments for dust entrainment and transport.

Our analyses also suggest a relatively widespread increase in MARs across most Ili Basin sites during the warming conditions of the global deglacial period (19–11 ka, Clark *et al.*, 2012) (Fig. 5a). Those sites which do not show any increase (KS15 and ZSP) are likely to be more influenced by their topographic setting; both are located in the easternmost or upper reaches of the basin with minimal exposure to Westerly air flow (and in general record very low accumulation rates). Elsewhere, short-lived phases of increased flux of coarser grain size fractions have been correlated to abrupt climatic events such as the Younger Dryas (*c.* 12–11 ka) at several sites during the deglacial period (e.g. NLK: Li *et al.*, 2018c; XEBLK: Li *et al.*, 2016b), and have been hypothesised to associate with increased Westerly penetration eastward into the Ili Basin. Climate simulations (Wyrwoll *et al.*, 2016) suggest that the strength of the Siberian High was reduced at this time. Such conditions would have increased the influence of the Westerlies on the Ili Basin, including increasing rainfall; increased deglacial moisture availability is supported by more dominant C_3 vegetation signatures in the basin (Ran and Feng, 2013). We suggest that sediment availability was greater than during the LGM due to increased runoff promoted both by glacial melt under warmer conditions and increased precipitation transported by the Westerlies.

Variability in loess accumulation rates across mid-latitude Asia: Implications for interpreting loess archives from Central Asia to the Chinese Loess Plateau

Continental mid-latitude Asia, with its extensive deserts and widespread loess deposits, is believed to be one of the major contributors to the global dust cycle (Narisma *et al.*, 2007; Kok *et al.*, 2021). It is therefore imperative that we understand the processes driving dust flux and their contribution to Northern Hemisphere climate dynamics. One major step towards our understanding of these processes involves quantifying Quaternary dust accumulation. Loess MARs provide the closest approximation of the 'dust parameter' over Pleistocene timescales. Given the issues raised by our analysis of the Ili Basin piedmont deposits, we compared loess MARs elsewhere in continental mid-latitude Asia over the same time period (0–60 ka), with a focus on the CLP and published sites across ACA more widely. In doing so we further assess spatial and temporal inhomogeneity in loess MARs and the degree to which regional characteristics such as topography and climate influence MARs.

The CLP of central northern China was the first loess region to be recognised as a significant terrestrial palaeoclimate archive (Liu, 1962), and is now one of the most intensively studied loess areas in the world (An *et al.*, 1991a,b; Porter and An, 1995; Ding *et al.*, 2002; Kohfeld and Harrison, 2003; Sun and An, 2005; Stevens *et al.*, 2008, 2013, 2018). Unlike the

Central Asian piedmonts, the CLP forms an extensive, continuous plateau exceeding 200 m thickness in parts and centred on the southern half of the Ordos Loop of the Yellow River (Yang and Ding, 2010). The loess is believed to derive from denudation associated with uplift of the Tibetan highlands (Sun and Liu, 2000; Sun, 2002; Smalley *et al.*, 2014); its connection with the ice sheets of the Tibetan 'third pole' underpins the assumption linking primary loess with glacial phases. The dominant sources of loess to the CLP are sediments derived from the Tibetan plateau, transported by the Yellow River prior to entrainment as dust (Stevens *et al.*, 2013; Nie *et al.*, 2015, 2018; Bird *et al.*, 2015, 2020); a significant proportion is recycled along the length of the river system as it flows along the plateau (Licht *et al.*, 2016). The climate of the CLP is strongly influenced by the East Asian winter and summer monsoons (EAWM and EASM, respectively; Lu *et al.*, 2022). Northwesterly winds associated with the Siberian High Pressure system produce cold, dry, dust-bearing EAWM winter conditions (Liu and Ding, 1998; Maher, 2016), which alternate with rain-bearing southeasterly EASM summer monsoonal air flow (An *et al.*, 1991b; Yang *et al.*, 2015). Grain-size analyses suggest that loess particles coarsen with strengthening EAWM during glacial conditions (Sun *et al.*, 2012; Stevens *et al.*, 2018). Several studies report a southeastward decrease in loess flux which correlates with decreasing grain size, and has been linked to the strength of the EAWM (Lu and Sun, 2000; Vriend *et al.*, 2011; Liu *et al.*, 2020). However, several high-resolution luminescence dating studies challenge the prevailing assumption that CLP loess accumulation is uniformly driven by the strength of the EAWM (Stevens *et al.*, 2006, 2007; Xu *et al.*, 2018).

Fig. 5c shows MARs from 11 selected sites (Lai and Wintle, 2006; Lai *et al.*, 2007; Lu *et al.*, 2007 Stevens *et al.*, 2008, 2016; Buylaert *et al.*, 2008; Sun *et al.*, 2012; Kang *et al.*, 2013; Qiu and Zhou, 2015; Fig. 4b) across the CLP, following a northwest–southeast (NW–SE) transect over the period *c.* 0–60 ka. We observe a distinct difference in net loess accumulation, as well as in the timing in peak MARs, between the northwestern and southeastern sites. MARs in the northwestern sites are approximately three times higher than those in the southeast.

As we observed for the sites in the Ili Basin, the geomorphic context in the CLP appears to influence both absolute accumulation and the timing of peaks in accumulation at individual sites. For example, among northwestern sites, JY shows higher accumulation rates than ZJC and GL, and likely relates to the proximity to the Yellow River; JY is located on the upper terraces of the river, whereas ZJC and GL are both situated further from fluvial source, south and north of the river, respectively. In contrast to the generally low accumulation rates of the southeastern sector, the site of MN, located on the banks of the Yellow River, has net accumulation comparable to the northwestern sites (Qiu and Zhou, 2015; see Figs. 4b and 5c). In general, sites in close proximity to the Yellow River, as well as those close to the desert deflation zones, record higher MARs than those more distal to these likely sources. It appears that despite the role of the EAWM as a dust transport vector (Vriend *et al.*, 2011; Liu *et al.*, 2020), net accumulation of loess across the CLP is also locally influenced by proximity to source sediment, whether fluvial or aeolian. Nevertheless, desert marginal sites, such as Jingbian (Stevens *et al.*, 2018), also record erosional unconformities; this effect has been proposed to result from increased erosional capacity of the EAWM in those regions. Not all records of MARs can be easily explained by climate mechanisms or by geomorphic context, however; the extremely high MAR at BGY during LGM (Fig. 5c) may relate to local preservation potential associated with expansion and contraction of the EASM (Buylaert *et al.*, 2008).

The timing of MAR peaks in aggregate across the CLP gives a more nuanced insight into the climate dynamics acting in the region than previously obtained. We observe a divergence in the timing of peaks in loess accumulation between the northwest and southeast. In the northwest, loess accumulation increases during *c.* 18–11 ka and decreases at *c.* 11–6 ka (Fig. 5c), whereas the opposite is observed in the southeastern sites. This alternating pattern has previously been attributed to a persistent weakening of the EAWM and gradual strengthening of the EASM during the early Holocene, with the opposite proposed for the deglacial (Xu *et al.*, 2018; Kang *et al.*, 2020). We suggest that the increase in MARs of the CLP southeastern sites during early Holocene may relate to their proximity to the Wei River, which drains the Qinling Mountains and is more strongly influenced by the EASM; aeolian flux in this region would therefore respond more closely to sediment availability relating to increased runoff during strengthened monsoon conditions. Overall, the CLP experienced an increase in MARs during the LGM and is consistent with widespread glaciation on the Tibetan Plateau (Owen *et al.*, 2003a,b, 2006; Owen and Dortsch, 2014), although relative changes in the southeastern sites was less pronounced, likely due to distance from the Yellow River and northern deserts. Loess MARs decreased altogether during MIS 3 (*c.* 57–29 ka, Lisiecki and Raymo, 2005), most likely due to relatively weakened EAWM wind strength, although sediment supply was sustained by suspended load fluvial outwash linked to glaciations on the Tibetan plateau (Owen *et al.*, 2003a; Owen and Dortch, 2014; Rother *et al.*, 2017) in response to increased monsoonal precipitation. Local preservation effects of vegetation during warmer interglacial periods may have also contributed to the decrease in sedimentation rates. Nonetheless, the sustained supply of sediment to the CLP can be observed in the generally higher MARs at the northwestern sites proximal to the river.

In addition to our analyses of MARs across the Ili Basin and CLP, we also calculated MARs from eight other published loess sites across ACA (Figs. 4a and 5b). These sites not only represent piedmont settings similar to those found in the Ili Basin but are also influenced by similar climatic contexts. The westernmost sites of BSK (Youn *et al.*, 2014) and VAL (Fitzsimmons *et al.*, 2017) lie in the foothills of the Kyrgyz Tien Shan and Karatau Range, respectively (Fig. 4a). The sites of LJW10 (Li *et al.*, 2015), SCZ17 (Duan *et al.*, 2020) and BYH10 (Li *et al.*, 2016a) are located along the northern piedmonts of the eastern Tian Shan, south of the Junggar Basin (and the Gurbantunggut desert), and TC and YM are situated in the westward opening Tacheng Basin, bound by the northern edge of the Dzungarian Alatau and the Tarbagatai Range to the north (Fig. 4a; Li *et al.*, 2019b).

As observed elsewhere, both absolute MAR values and the timing of peak accumulation are highly variable across the greater ACA. In the west, BSK experienced increased accumulation during late MIS 3, continuing into the LGM, while VAL yields substantially lower MARs which remained consistent from late MIS 3 into the LGM. The higher accumulation rates at BSK are most likely due to its proximity to the glacially derived Chu River. Glacial expansion in the Kyrgyz Tien Shan during MIS 3 (Koppes *et al.*, 2008) likely generated the fine-grained sediment for loess deposition at BSK, whereas the Karatau Range, from which the VAL sediments were sourced, was never glaciated and is much more arid, resulting in substantially less sediment supply. Both Tacheng Basin sites yield low, almost constant MARs (*c.* 30-40 g $cm^{-2}ka^{-1}$) throughout the past *c.* 60 ky (Li *et al.*, 2019b). It is likely that these records relate to the lack of glaciation in the surrounding mountains, resulting in a dependence on the desert to the west as a source of dust (Li *et al*., 2019b). By contrast, the sites located in the Northern Tien Shan foothills yield variable depositional characteristics (Figs. 4a and 5b). The site of QS-16 yielded an LGM peak in accumulation; by comparison, the site of BYH-10, located further east, experienced peak MARs from early to mid-MIS 3 an order of magnitude greater than at QS-16, followed by a hiatus and subsequent LGM MAR values comparable with QS-16. LGM deposition in the northern Tien Shan area has been linked to regionally arid conditions and strengthened Westerlies which increased aeolian flux (Li *et al*., 2016a, 2020). The substantial difference in absolute MAR values at BYH-10 and QS-16 is most likely linked to their individual topographic and geomorphic setting; the former is located on the exposed northern piedmont of the Bogda Shan (eastern Tien Shan) which drains a number of glacially fed rivers, whereas QS-16 is sheltered from the prevailing westerly winds by the Borohoro mountains and is at a greater distance from the northern dust source regions.

It is clear from our MAR review of the Ili Basin, wider ACA and CLP that absolute accumulation rates and timing at a given site may be influenced by both synoptic-scale climate and local geomorphic settings in the form of proximity to dust sources, topography and sediment availability. Here, it is important to emphasise the influence of post-depositional erosion on sedimentation rates at a site; which in an aeolian context, is implicitly controlled by the topographic setting as well as local climatic conditions at the site. Notwithstanding, our review suggests that the timing of peaks in loess accumulation as an aggregate of multiple sites represents a reliable response to climate.

CONCLUSION

This study provides high-resolution chronological frameworks for five new loess sites in the vastly understudied piedmonts of the Zailisky Alatau (Central Tien Shan). Our new dataset provides the spatial coverage necessary to interrogate the timing and rate of loess deposition along the Ili Basin piedmonts as a whole, whereas previously only the eastern part of the basin and isolated western sites could be analysed. We observe substantial variability in the timing and rate of loess deposition across our new sites, which raises questions regarding the degree to which the timing and rate of accumulation at individual sites can be taken as an indicator of past climate in this region. Our observations across the Ili Basin as a whole indicate a patchwork of loess deposition. Absolute sedimentation rates at a given site respond both to local topographic context and sediment availability and to climate. The timing of peaks in accumulation, irrespective of absolute MAR values and particularly when viewed in aggregate across a number of sites, represent a response to variability in wind dynamics driven by the Northern Hemispheric climate subsystems. This interpretation was supported by our analyses of MARs from loess sites across wider ACA and the CLP over the past 60 ka. We find that aggregate MARs from multiple sites provide a more robust tool for understanding past climate dynamics across a region and overcome individual site bias.

ACKNOWLEDGEMENTS. AK Dave would like to gratefully acknowledge the following persons and institutions for their support: Steffi Hesse and Victoria Krippner at the Max Planck Institute for Evolutionary Anthropology (MPI-EVA), Leipzig, Germany, for access to the HF laboratory, Dr Zoran Perić at the Max Planck Institute for Chemistry and Dr Giovanni Muttoni for the use of magnetic susceptibility measurement facilities at the Alpine Palaeomagnetism Laboratory (Peveragno, Italy). Thanks also to A. Umarkhojiyev, A. Kossenko and A. Sirch for assistance in the field. L. Lisá acknowledges the support of internal programme No. RVO67985831 of the Institute of Geology CAS, Prague, and OP RDE, MEYS under the project 'Ultra-trace isotope research in social and environmental studies using accelerator mass spectrometry', Reg. No. CZ.02.1.01/0.0/0.0/16_019/0000728. This study was funded by an independent Max Planck Research Group awarded by the Max Planck Society to KE Fitzsimmons. Open Access funding enabled and organized by Projekt DEAL.

Data availability statement

The data that support the findings of this study are available from the corresponding author upon reasonable request.

Author contributions—**Aditi K. Dave**: Conceptualization; Investigation; Writing – original draft; Visualization; Writing – review & editing; Validation; Methodology; Software; Formal analysis. **Lenka Lisá**: Methodology; Writing – review & editing. **Giancarlo Scardia**: Methodology; Writing – review & editing. **Saida Nigmatova**: Data curation; Resources; Writing – review & editing. **Kathryn E. Fitzsimmons**: Conceptualization; Writing – review & editing; Project administration; Supervision; Funding acquisition; Methodology.

Supporting information

Additional supporting information can be found in the online version of this article.

REFERENCES

Albani S, Mahowald NM. 2019. Paleodust Insights into Dust Impacts on Climate. *Journal of Climate* **32**(22): 7897–7913. https://doi.org/10.1175/JCLI-D-18-0742.1

An ZhiSheng, Kukla G, Porter SC, Xiao J. 1991a. Late quaternary dust flow on the Chinese Loess Plateau. *Catena* **18**(2): 125–132. https://doi.org/10.1016/0341-8162(91)90012-M

An Zhisheng, Kukla GJ, Porter SC, Xiao J. 1991b. Magnetic susceptibility evidence of monsoon variation on the Loess Plateau of central China during the last 130,000 years. *Quaternary Research* **36**(1): 29–36. https://doi.org/10.1016/0033-5894(91)90015-W

Andreae MO, Rosenfeld D. 2008. Aerosol–cloud–precipitation interactions. Part 1. The nature and sources of cloud-active aerosols. *Earth-Science Reviews* **89**(1): 13–41. https://doi.org/10.1016/j.earscirev.2008.03.001

Antoine P, Rousseau D-D, Moine O, Kunesch S, Hatté C, Lang A, Tissoux H, Zöller L. 2009. Rapid and cyclic aeolian deposition during the Last Glacial in European loess: A high-resolution record from Nussloch, Germany. *Quaternary Science Reviews* **28**(25): 2955–2973. https://doi.org/10.1016/j.quascirev.2009.08.001

Arimoto R. 2001. Eolian dust and climate: Relationships to sources, tropospheric chemistry, transport and deposition. *Earth-Science Reviews* **54**(1): 29–42. https://doi.org/10.1016/S0012-8252(01)00040-X

Banerjee D, Murray AS, Bøtter-Jensen L, Lang A. 2001. Equivalent dose estimation using a single aliquot of polymineral fine grains. *Radiation Measurements* **33**(1): 73–94. https://doi.org/10.1016/S1350-4487(00)00101-3

Berger A, Loutre MF. 1991. Insolation values for the climate of the last 10 million years. *Quaternary Science Reviews* **10**(4): 297–317. https://doi.org/10.1016/0277-3791(91)90033-Q

Bird A, Stevens T, Rittner M, Vermeesch P, Carter A, Andò S, Garzanti E, Lu H, Nie J, Zeng L, Zhang H, Xu Z. 2015. Quaternary dust source variation across the Chinese Loess Plateau. *Palaeogeography, Palaeoclimatology, Palaeoecology* **435**: 254–264. https://doi.org/10.1016/j.palaeo.2015.06.024

Bird A, Millar I, Rodenburg T, Stevens T, Rittner M, Vermeesch P, Lu H. 2020. A constant Chinese Loess Plateau dust source since the late

Miocene. *Quaternary Science Reviews* **227**: 106042. https://doi.org/10.1016/j.quascirev.2019.106042

Blaauw M, Christen JA. 2011. Flexible paleoclimate age-depth models using an autoregressive gamma process. *Bayesian Analysis* **6**(3): 457–474. https://doi.org/10.1214/11-BA618

Blomdin R, Stroeven AP, Harbor JM, Lifton NA, Heyman J, Gribenski N, Petrakov DA, Caffee MW, Ivanov MN, Hättestrand C, Rogozhina I, Usubaliev R. 2016. Evaluating the timing of former glacier expansions in the Tian Shan: A key step towards robust spatial correlations. *Quaternary Science Reviews* **153**: 78–96. https://doi.org/10.1016/j.quascirev.2016.07.029

Blott SJ, Pye K. 2001. GRADISTAT: A grain size distribution and statistics package for the analysis of unconsolidated sediments. *Earth Surface Processes and Landforms* **26**(11): 1237–1248. https://doi.org/10.1002/esp.261

Buylaert JP, Murray AS, Vandenberghe D, Vriend M, Corte FD, den haute PV. 2008. Optical dating of Chinese loess using sand-sized quartz: Establishing a time frame for Late Pleistocene climate changes in the western part of the Chinese Loess Plateau. *Quaternary Geochronology* **3**(1): 99–113. https://doi.org/10.1016/j.quageo.2007.05.003

Chen Y, Li Y, Wang Y, Zhang M, Cui Z, Yi C, Liu G. 2015. Late Quaternary glacial history of the Karlik Range, easternmost Tian Shan, derived from 10Be surface exposure and optically stimulated luminescence datings. *Quaternary Science Reviews* **115**: 17–27. https://doi.org/10.1016/j.quascirev.2015.02.010

Cheng L, Song Y, Wu Y, Liu Y, Liu H, Chang H, Zong X, Kang S. 2021. Drivers for asynchronous patterns of dust accumulation in central and eastern Asia and in Greenland during the last glacial maximum. *Geophysical Research Letters* **48**: e2020GL091194. https://doi.org/10.1029/2020GL091194

ChongYi E, Lai Z, Sun Y, Hou G, Yu L, Wu C. 2012. A luminescence dating study of loess deposits from the Yili River basin in western China. *Quaternary Geochronology* **10**: 50–55. https://doi.org/10.1016/j.quageo.2012.04.022

Clark PU, Dyke AS, Shakun JD, Carlson AE, Clark J, Wohlfarth B, Mitrovica JX, Hostetler SW, McCabe AM. 2009. The Last Glacial Maximum. *Science* **325**(5941): 710. https://doi.org/10.1126/science.1172873

Clark PU, Shakun JD, Baker PA, Bartlein PJ, Brewer S, Brook E, Carlson AE, Cheng H, Kaufman DS, Liu Z, Marchitto TM, Mix AC, Morrill C, Otto-Bliesner BL, Pahnke K, Russell JM, Whitlock C, Adkins JF, Blois JL, Williams JW. 2012. Global climate evolution during the last deglaciation. *Proceedings of the National Academy of Sciences* **109**(19): E1134. https://doi.org/10.1073/pnas.1116619109

Dave AK, Courty M-A, Fitzsimmons KE, Singhvi AK. 2019. Revisiting the contemporaneity of a mighty river and the Harappans: Archaeological, stratigraphic and chronometric constraints. *Quaternary Geochronology* **49**: 230–235. https://doi.org/10.1016/j.quageo.2018.05.002

Ding Z, Liu T, Rutter NW, Yu Z, Guo Z, Zhu R. 1995. Ice-Volume Forcing of East Asian Winter Monsoon Variations in the Past 800,000 Years. *Quaternary Research* **44**(2): 149–159. Cambridge Core https://doi.org/10.1006/qres.1995.1059

Ding ZL, Derbyshire E, Yang SL, Yu ZW, Xiong SF, Liu TS. 2002. Stacked 2.6-Ma grain size record from the Chinese loess based on five sections and correlation with the deep-sea δ18O record. *Paleoceanography* **17**(3): 5–1-5–21. https://doi.org/10.1029/2001PA000725

Duan F, An C, Wang W, Herzschuh U, Zhang M, Zhang H, Liu Y, Zhao Y, Li G. 2020. Dating of a late Quaternary loess section from the northern slope of the Tianshan Mountains (Xinjiang, China) and its paleoenvironmental significance. *Quaternary International* **544**: 104–112. https://doi.org/10.1016/j.quaint.2020.02.034

Feng ZD, Ran M, Yang QL, Zhai XW, Wang W, Zhang XS, Huang CQ. 2011. Stratigraphies and chronologies of late Quaternary loess–paleosol sequences in the core area of the central Asian arid zone. *Quaternary International* **240**: 156–166. https://doi.org/10.1016/j.quaint.2010.10.019

Fenn K, Durcan JA, Thomas DSG, Banak A. 2020. A 180 ka record of environmental change at Erdut (Croatia): A new chronology for the loess–palaeosol sequence and its implications for environmental interpretation. *Journal of Quaternary Science* **35**(4): 582–593. https://doi.org/10.1002/jqs.3201

Fitzsimmons KE, Marković SB, Hambach U. 2012. Pleistocene environmental dynamics recorded in the loess of the middle and lower Danube basin. *Quaternary Science Reviews* **41**: 104–118. https://doi.org/10.1016/j.quascirev.2012.03.002

Fitzsimmons KE, Hambach U. 2014. Loess accumulation during the last glacial maximum: Evidence from Urluia, southeastern Romania. *Quaternary International* **334–335**: 74–85. https://doi.org/10.1016/j.quaint.2013.08.005

Fitzsimmons KE. 2017. Reconstructing palaeoenvironments on desert margins: New perspectives from Eurasian loess and Australian dry lake shorelines. *Quaternary Science Reviews* **171**: 1–19. https://doi.org/10.1016/j.quascirev.2017.05.018

Fitzsimmons KE, Iovita R, Sprafke T, Glantz M, Talamo S, Horton K, Beeton T, Alipova S, Bekseitov G, Ospanov Y, Deom J-M, Sala R, Taimagambetov Z. 2017. A chronological framework connecting the early Upper Palaeolithic across the Central Asian piedmont. *Journal of Human Evolution* **113**: 107–126. https://doi.org/10.1016/j.jhevol.2017.07.006

Fitzsimmons KE, Sprafke T, Zielhofer C, Günter C, Deom J-M, Sala R, Iovita R. 2018. Loess accumulation in the Tian Shan piedmont: Implications for palaeoenvironmental change in arid Central Asia. *Quaternary International* **469**: 30–43. https://doi.org/10.1016/j.quaint.2016.07.041

Fitzsimmons KE, Nowatzki M, Dave AK, Harder H. 2020. Intersections between wind regimes, topography and sediment supply: Perspectives from aeolian landforms in Central Asia. *Palaeogeography, Palaeoclimatology, Palaeoecology* **540**: 109531. https://doi.org/10.1016/j.palaeo.2019.109531

Frechen M, Schweitzer U, Zander A. 1996. Improvements in sample preparation for the fine grain technique. *Ancient TL* **14**(2): 15–17.

Grützner C, Walker RT, Abdrakhmatov KE, Mukambaev A, Elliott AJ, Elliott JR. 2017. Active Tectonics Around Almaty and along the Zailisky Alatau Rangefront. *Tectonics* **36**(10): 2192–2226. https://doi.org/10.1002/2017TC004657

Guérin G, Mercier N, Adamiec G. 2011. Dose-rate conversion factors: Update. *Ancient TL* **29**(1): 5–8.

Hao Q, Wang L, Oldfield F, Peng S, Qin L, Song Y, Xu B, Qiao Y, Bloemendal J, Guo Z. 2012. Delayed build-up of Arctic ice sheets during 400,000-year minima in insolation variability. *Nature* **490**(7420): 393–396. https://doi.org/10.1038/nature11493

Jain M, Singhvi AshokK. 2001. Limits to depletion of blue-green light stimulated luminescence in feldspars: Implications for quartz dating. *Radiation Measurements* **33**(6): 883–892. https://doi.org/10.1016/S1350-4487(01)00104-4

Jia J, Liu H, Gao F, Xia D. 2018. Variations in the westerlies in Central Asia since 16 ka recorded by a loess section from the Tien Shan Mountains. *Palaeogeography, Palaeoclimatology, Palaeoecology* **504**: 156–161. https://doi.org/10.1016/j.palaeo.2018.05.021

Kang S, Wang X, Lu Y. 2013. Quartz OSL chronology and dust accumulation rate changes since the Last Glacial at Weinan on the southeastern Chinese Loess Plateau: Quartz OSL chronology and dust accumulation rates, SE Chinese Loess Plateau. *Boreas* **42**: 815–829. https://doi.org/10.1111/bor.12005

Kang S, Wang X, Lu Y, Liu W, Song Y, Wang N. 2015. A high-resolution quartz OSL chronology of the Talede loess over the past ~30 ka and its implications for dust accumulation in the Ili Basin, Central Asia. *Quaternary Geochronology* **30**: 181–187. https://doi.org/10.1016/j.quageo.2015.04.006

Kang S, Du J, Wang N, Dong J, Wang D, Wang X, Qiang X, Song Y. 2020. Early Holocene weakening and mid- to late Holocene strengthening of the East Asian winter monsoon. *Geology* **48**(11): 1043–1047. https://doi.org/10.1130/G47621.1

Kohfeld KE, Harrison SP. 2000. How well can we simulate past climates? Evaluating the models using global palaeoenvironmental datasets. *Quaternary Science Reviews* **19**(1–5): 321–346. https://doi.org/10.1016/S0277-3791(99)00068-2

Kohfeld KE, Harrison SP. 2003. Glacial-interglacial changes in dust deposition on the Chinese Loess Plateau. *Quaternary Science Reviews* **22**(18): 1859–1878. https://doi.org/10.1016/S0277-3791(03)00166-5

Kok JF, Adebiyi AA, Albani S, Balkanski Y, Checa-Garcia R, Chin M, Colarco PR, Hamilton DS, Huang Y, Ito A, Klose M, Li L, Mahowald NM, Miller RL, Obiso V, Pérez García-Pando C, Rocha-Lima A, Wan JS. 2021. Contribution of the world's main dust source regions to the global cycle of desert dust. *Atmospheric Chemistry and Physics Discussions* **2021**: 1–34. https://doi.org/10.5194/acp-2021-4

Konert M, Vandenberghe J. 1997. Comparison of laser grain size analysis with pipette and sieve analysis: A solution for the underestimation of the clay fraction. *Sedimentology* **44**(3): 523–535. https://doi.org/10.1046/j.1365-3091.1997.d01-38.x

Kong P, Fink D, Na C, Huang F. 2009. Late Quaternary glaciation of the Tianshan, Central Asia, using cosmogenic 10Be surface exposure dating. *Quaternary Research* **72**(2): 229–233. https://doi.org/10.1016/j.yqres.2009.06.002

Koppes M, Gillespie AR, Burke RM, Thompson SC, Stone J. 2008. Late Quaternary glaciation in the Kyrgyz Tien Shan. *Quaternary Science Reviews* **27**(7): 846–866. https://doi.org/10.1016/j.quascirev.2008.01.009

Kukla G, Heller F, Ming LX, Chun XT, Sheng LT, Sheng AZ. 1988. Pleistocene climates in China dated by magnetic susceptibility. *Geology* **16**(9): 811–814. https://doi.org/10.1130/0091-7613(1988)016<0811:PCICDB>2.3.CO;2

Lai Z, Wintle AG, Thomas DSG. 2007. Rates of dust deposition between 50 ka and 20 ka revealed by OSL dating at Yuanbao on the Chinese Loess Plateau. *Palaeogeography, Palaeoclimatology, Palaeoecology* **248**(3): 431–439. https://doi.org/10.1016/j.palaeo.2006.12.013

Lai Z-P, Wintle AG. 2006. Locating the boundary between the Pleistocene and the Holocene in Chinese loess using luminescence. *The Holocene* **16**(6): 893–899. https://doi.org/10.1191/0959683606hol980rr

Li Yingkui, Liu G, Kong P, Harbor J, Chen Y, Caffee M. 2011. Cosmogenic nuclide constraints on glacial chronology in the source area of the Urumqi River, Tian Shan, China. *Journal of Quaternary Science* **26**(3): 297–304. https://doi.org/10.1002/jqs.1454

Li Yingkui, Liu G, Chen Y, Li Y, Harbor J, Stroeven AP, Caffee M, Zhang M, Li C, Cui Z. 2014. Timing and extent of Quaternary glaciations in the Tianger Range, eastern Tian Shan, China, investigated using 10Be surface exposure dating. *Quaternary Science Reviews* **98**: 7–23. https://doi.org/10.1016/j.quascirev.2014.05.009

Li G, Wen L, Xia D, Duan Y, Rao Z, Madsen DB, Wei H, Li F, Jia J, Chen F. 2015. Quartz OSL and K-feldspar pIRIR dating of a loess/paleosol sequence from arid central Asia, Tianshan Mountains, NW China. *Quaternary Geochronology* **28**: 40–53. https://doi.org/10.1016/j.quageo.2015.03.011

Li Guoqiang, Rao Z, Duan Y, Xia D, Wang L, Madsen DB, Jia J, Wei H, Qiang M, Chen J, Chen F. 2016a. Paleoenvironmental changes recorded in a luminescence dated loess/paleosol sequence from the Tianshan Mountains, arid central Asia, since the Penultimate Glaciation. *Earth and Planetary Science Letters* **448**: 1–12. https://doi.org/10.1016/j.epsl.2016.05.008

Li Yun, Song Y, Lai Z, Han L, An Z. 2016b. Rapid and cyclic dust accumulation during MIS 2 in Central Asia inferred from loess OSL dating and grain-size analysis. *Scientific Reports* **6**(1): 32365. https://doi.org/10.1038/srep32365

Li Guoqiang, Chen F, Xia D, Yang H, Zhang X, Madsen D, Oldknow C, Wei H, Rao Z, Qiang M. 2018a. A Tianshan Mountains loess-paleosol sequence indicates anti-phase climatic variations in arid central Asia and in East Asia. *Earth and Planetary Science Letters* **494**: 153–163. https://doi.org/10.1016/j.epsl.2018.04.052

Li Yue, Song Y, Fitzsimmons KE, Chen X, Wang Q, Sun H, Zhang Z. 2018b. New evidence for the provenance and formation of loess deposits in the Ili River Basin, Arid Central Asia. *Aeolian Research* **35**: 1–8. https://doi.org/10.1016/j.aeolia.2018.08.002

Li Y, Song Y, Fitzsimmons KE, Chang H, Orozbaev R, Li X. 2018c. Eolian dust dispersal patterns since the last glacial period in eastern Central Asia: Insights from a loess-paleosol sequence in the Ili Basin. *Climate of the Past* **14**(3): 271–286. https://doi.org/10.5194/cp-14-271-2018

Li Yue, Song Y, Qiang M, Miao Y, Zeng M. 2019a. Atmospheric Dust Variations in the Ili Basin, Northwest China, During the Last Glacial Period as Revealed by a High Mountain Loess-Paleosol Sequence. *Journal of Geophysical Research: Atmospheres* **124**(15): 8449–8466. https://doi.org/10.1029/2019JD030470

Li Y, Song Y, Yin Q, Han L, Wang Y. 2019b. Orbital and millennial northern mid-latitude westerlies over the last glacial period. *Climate Dynamics* **53**(5–6): 3315–3324. https://doi.org/10.1007/s00382-019-04704-5

Li Guoqiang, Yang H, Stevens T, Zhang X, Zhang H, Wei H, Zheng W, Li L, Liu X, Chen J, Xia D, Oldknow C, Ye W, Chen F. 2020. Differential ice volume and orbital modulation of Quaternary moisture patterns between Central and East Asia. *Earth and Planetary Science Letters* **530**: 115901. https://doi.org/10.1016/j.epsl.2019.115901

Licht A, Dupont-Nivet G, Pullen A, Kapp P, Abels HA, Lai Z, Guo Z, Abell J, Giesler D. 2016. Resilience of the Asian atmospheric circulation shown by Paleogene dust provenance. *Nature Communications* **7**(1): 12390. https://doi.org/10.1038/ncomms12390

Lifton N, Beel C, Hättestrand C, Kassab C, Rogozhina I, Heermance R, Stroeven AP. 2014. Constraints on the late Quaternary glacial history of the Inylchek and Sary-Dzaz valleys from in situ cosmogenic 10Be and 26Al, eastern Kyrgyz Tian Shan. *Quaternary Science Reviews* **101**: 77–90. https://doi.org/10.1016/j.quascirev.2014.06.032

Lisiecki LE, Raymo ME. 2005. A Pliocene-Pleistocene stack of 57 globally distributed benthic δ18O records. *Paleoceanography* **20**: PA1003. https://doi.org/10.1029/2004PA001071

Liu T. 1962. The huangtu (loess) of China. *Acta Geol. Sinica* **42**: 1–14.

Liu TS. 1985. *Loess and Environment*. China Ocean Press: Beijing.

Liu T, Ding Z. 1998. Chinese loess and the paleomonsoon. *Annual Review of Earth and Planetary Sciences* **26**(1): 111–145. https://doi.org/10.1146/annurev.earth.26.1.111

Liu Y, Liu X, Ma L, Kang S, Qiang X, Guo F, Sun Y. 2020. Temporal–spatial variations in aeolian flux on the Chinese Loess Plateau during the last 150 ka. *Geological Magazine* **157**(5): 757–767. https://doi.org/10.1017/S0016756819001067

Łomotowski, J, Burszta-Adamiak, E, Kęszycka, M, Jary, Z. 2008. In: Metody i techniki optyczne w badaniach zawiesin, Badania Sy. Instytut Badań Systemowych PAN, Warszawa. (n.d.).

Lu H, Sun D. 2000. Pathways of dust input to the Chinese Loess Plateau during the last glacial and interglacial periods. *Catena* **40**(3): 251–261. https://doi.org/10.1016/S0341-8162(00)00090-4

Lu YC, Wang XL, Wintle AG. 2007. A new OSL chronology for dust accumulation in the last 130,000 yr for the Chinese Loess Plateau. *Quaternary Research* **67**(1): 152–160. https://doi.org/10.1016/j.yqres.2006.08.003

Lu H, Wang X, Wang Y, Zhang X, Yi S, Wang X, Stevens T, Kurbanov R, Marković SB. 2022. Chinese Loess and the Asian Monsoon: What We Know and What Remains Unknown. *Quaternary International* **620**: 85–97. https://doi.org/10.1016/j.quaint.2021.04.027

Lydolph PE. 1977. *Climates of the Soviet Union*. Elsevier Scientific Pub. Co: Amsterdam; New York.

Machalett B, Frechen M, Hambach U, Oches EA, Zöller L, Marković SB. 2006. The loess sequence from Remisowka (northern boundary of the Tien Shan Mountains, Kazakhstan)—Part I: Luminescence dating. *Quaternary International* **152–153**: 192–201. https://doi.org/10.1016/j.quaint.2005.12.014

Machalett B, Oches EA, Frechen M, Zöller L, Hambach UF, Mavlyanova N, Marković S, Endlicher WR. 2008. Aeolian dust dynamics in central Asia during the Pleistocene: Driven by the long-term migration, seasonality, and permanency of the Asiatic polar front. *Geochemistry, Geophysics, Geosystems* **9**: Q08Q09. https://doi.org/10.1029/2007GC001938

Maher BA. 2016. Palaeoclimatic records of the loess/palaeosol sequences of the Chinese Loess Plateau. *Quaternary Science Reviews* **154**: 23–84. https://doi.org/10.1016/j.quascirev.2016.08.004

Marković SB, Stevens T, Kukla GJ, Hambach U, Fitzsimmons KE, Gibbard P, Svirčev Z. 2015. Danube loess stratigraphy—Towards a pan-European loess stratigraphic model. *Earth-Science Reviews* **148**: 228–258. https://doi.org/10.1016/j.earscirev.2015.06.005

Martin JH. 1990. Glacial-interglacial CO_2 change: The Iron Hypothesis. *Paleoceanography* **5**(1): 1–13. https://doi.org/10.1029/PA005i001p00001

Martínez-García A, Sigman DM, Ren H, Anderson RF, Straub M, Hodell DA, Haug GH. 2014. Iron Fertilization of the Subantarctic

Ocean During the Last Ice Age. *Science* **343**(6177): 1347. https://doi.org/10.1126/science.1246848
Muhs DR. 2007. Loess deposits, origins and properties, *Encyclopedia of Quaternary Science*. Elsevier, 1405–1418. https://doi.org/10.1016/B0-44-452747-8/00158-7
Murray AS, Wintle AG. 2000. Luminescence dating of quartz using an improved single-aliquot regenerative-dose protocol. *Radiation Measurements* **32**(1): 57–73. https://doi.org/10.1016/S1350-4487(99)00253-X
Murray AS, Wintle AG. 2003. The single aliquot regenerative dose protocol: Potential for improvements in reliability. *Radiation Measurements* **37**(4): 377–381. https://doi.org/10.1016/S1350-4487(03)00053-2
Narisma GT, Foley JA, Licker R, Ramankutty N. 2007. Abrupt changes in rainfall during the twentieth century. *Geophysical Research Letters* **34**: L06710. https://doi.org/10.1029/2006GL028628
Nie J, Stevens T, Rittner M, Stockli D, Garzanti E, Limonta M, Bird A, Andò S, Vermeesch P, Saylor J, Lu H, Breecker D, Hu X, Liu S, Resentini A, Vezzoli G, Peng W, Carter A, Ji S, Pan B. 2015. Loess Plateau storage of Northeastern Tibetan Plateau-derived Yellow River sediment. *Nature Communications* **6**(1): 8511. https://doi.org/10.1038/ncomms9511
Nie J, Pullen A, Garzione CN, Peng W, Wang Z. 2018. Pre-Quaternary decoupling between Asian aridification and high dust accumulation rates. *Science Advances* **4**(2): eaao6977. https://doi.org/10.1126/sciadv.aao6977
Obruchev VA. 1945. Loess types and their origin. *American Journal of Science* **243**(5): 256–262. https://doi.org/10.2475/ajs.243.5.256
Owen LA, Finkel RC, Haizhou M, Spencer JQ, Derbyshire E, Barnard PL, Caffee MW. 2003a. Timing and style of Late Quaternary glaciation in northeastern Tibet. *Geological Society of America Bulletin* **115**(11): 1356. https://doi.org/10.1130/B25314.1
Owen LA, Ma H, Derbyshire E, Spencer JQ, Barnard PL, Zeng YN, Caffee MW. 2003b. The timing and style of Late Quaternary glaciation in the La Ji Mountains, NE Tibet: Evidence for restricted glaciation during the latter part of the Last Glacial. *Zeitschrift Fur Geomorphologie, Supplementband* **130**: 263–276.
Owen LA, Finkel RC, Haizhou M, Barnard PL. 2006. Late Quaternary landscape evolution in the Kunlun Mountains and Qaidam Basin, Northern Tibet: A framework for examining the links between glaciation, lake level changes and alluvial fan formation. *Quaternary International* **154–155**: 73–86. Scopus https://doi.org/10.1016/j.quaint.2006.02.008
Owen LA, Dortch JM. 2014. Nature and timing of Quaternary glaciation in the Himalayan–Tibetan orogen. *Quaternary Science Reviews* **88**: 14–54. https://doi.org/10.1016/j.quascirev.2013.11.016
Pécsi M. 1990. Loess is not just the accumulation of dust. *Quaternary International* **7–8**: 1–21. https://doi.org/10.1016/1040-6182(90)90034-2
Porter SC, An Z. 1995. Correlation between climate events in the North Atlantic and China during the last glaciation. *Nature* **375**(6529): 305–308. https://doi.org/10.1038/375305a0
Prescott JR, Hutton JT. 1994. Cosmic ray contributions to dose rates for luminescence and ESR dating: Large depths and long-term time variations. *Radiation Measurements* **23**(2): 497–500. https://doi.org/10.1016/1350-4487(94)90086-8
Pye K. 1987. *Aeolian Dust and Dust Deposits*. Academic Press: London.
Qiu F, Zhou L. 2015. A new luminescence chronology for the Mangshan loess-palaeosol sequence on the southern bank of the Yellow River in Henan, central China. *Quaternary Geochronology* **30**: 24–33. https://doi.org/10.1016/j.quageo.2015.06.014
Ran M, Feng Z. 2013. Holocene moisture variations across China and driving mechanisms: A synthesis of climatic records. *Quaternary International* **313–314**: 179–193. https://doi.org/10.1016/j.quaint.2013.09.034
Rasmussen SO, Bigler M, Blockley SP, Blunier T, Buchardt SL, Clausen HB, Winstrup M. 2014. A stratigraphic framework for abrupt climatic changes during the Last Glacial period based on three synchronized Greenland ice-core records: Refining and extending the INTIMATE event stratigraphy. *Quaternary Science Reviews* **106**: 14–28. https://doi.org/10.1016/j.quascirev.2014.09.007
Rother H, Stauch G, Loibl D, Lehmkuhl F, Freeman SPHT. 2017. Late Pleistocene glaciations at Lake Donggi Cona, eastern Kunlun Shan (NE Tibet): Early maxima and a diminishing trend of glaciation during the last glacial cycle. *Boreas* **46**(3): 503–524. https://doi.org/10.1111/bor.12227
Ruth U, Bigler M, Röthlisberger R, Siggaard-Andersen M-L, Kipfstuhl S, Goto-Azuma K, Hansson ME, Johnsen SJ, Lu H, Steffensen JP. 2007. Ice core evidence for a very tight link between North Atlantic and east Asian glacial climate. *Geophysical Research Letters* **34**: L03706. https://doi.org/10.1029/2006GL027876
Schaetzl RJ, Bettis EA, Crouvi O, Fitzsimmons KE, Grimley DA, Hambach U, Zech R. 2018. Approaches and challenges to the study of loess—Introduction to the LoessFest Special Issue. *Quaternary Research* **89**(3): 563–618. https://doi.org/10.1017/qua.2018.15
Schaffernicht EJ, Ludwig P, Shao Y. 2020. Linkage between dust cycle and loess of the Last Glacial Maximum in Europe. *Atmospheric Chemistry and Physics* **20**(8): 4969–4986. https://doi.org/10.5194/acp-20-4969-2020
Schulte P, Sprafke T, Rodrigues L, Fitzsimmons KE. 2018. Are fixed grain size ratios useful proxies for loess sedimentation dynamics? Experiences from Remizovka, Kazakhstan. *Aeolian Research* **31**(B): 131–140. https://doi.org/10.1016/j.aeolia.2017.09.002
Schurr B, Ratschbacher L, Sippl C, Gloaguen R, Yuan X, Mechie J. 2014. Seismotectonics of the Pamir. *Tectonics* **33**(8): 1501–1518. https://doi.org/10.1002/2014TC003576
Singhvi AK, Bluszcz A, Bateman MD, Rao MS. 2001. Luminescence dating of loess–palaeosol sequences and coversands: Methodological aspects and palaeoclimatic implications. *Recent Research on Loess and Palaeosols, Pure and Applied* **54**(1): 193–211. https://doi.org/10.1016/S0012-8252(01)00048-4
Smalley I. 1995. Making the material: The formation of silt sized primary mineral particles for loess deposits. *Quaternary Science Reviews* **14**(7): 645–651. https://doi.org/10.1016/0277-3791(95)00046-1
Smalley IJ, Kumar R, O'Hara Dhand K, Jefferson IF, Evans RD. 2005. The formation of silt material for terrestrial sediments: Particularly loess and dust. *Sedimentary Geology* **179**(3): 321–328. https://doi.org/10.1016/j.sedgeo.2005.06.011
Smalley I, O'Hara-Dhand K, Kwong J. 2014. China: Materials for a loess landscape. *Catena* **117**: 100–107. https://doi.org/10.1016/j.catena.2013.11.016
Song Yougui, Li C, Zhao J, Cheng P, Zeng M. 2012. A combined luminescence and radiocarbon dating study of the Ili loess, Central Asia. *Quaternary Geochronology* **10**: 2–7. https://doi.org/10.1016/j.quageo.2012.04.005
Song Yougui, Chen X, Qian L, Li C, Li Y, Li X, An Z. 2014. Distribution and composition of loess sediments in the Ili Basin, Central Asia. *Quaternary International* **334–335**: 61–73. https://doi.org/10.1016/j.quaint.2013.12.053
Song Yougui, Lai Z, Li Y, Chen T, Wang Y. 2015. Comparison between luminescence and radiocarbon dating of late Quaternary loess from the Ili Basin in Central Asia. *Quaternary Geochronology* **30**: 405–410. https://doi.org/10.1016/j.quageo.2015.01.012
Sprafke T, Fitzsimmons KE, Grützner C, Elliot A, Marquer L, Nigmatova S. 2018. Reevaluation of Late Pleistocene loess profiles at Remizovka (Kazakhstan) indicates the significance of topography in evaluating terrestrial paleoclimate records. *Quaternary Research* **89**(3): 674–690. https://doi.org/10.1017/qua.2017.103
Stevens Thomas, Armitage SJ, Lu H, Thomas DSG. 2006. Sedimentation and diagenesis of Chinese loess: Implications for the preservation of continuous, high-resolution climate records. *Geology* **34**(10): 849–852. https://doi.org/10.1130/G22472.1
Stevens Thomas, Thomas DSG, Armitage SJ, Lunn HR, Lu H. 2007. Reinterpreting climate proxy records from late Quaternary Chinese loess: A detailed OSL investigation. *Earth-Science Reviews* **80**(1): 111–136. https://doi.org/10.1016/j.earscirev.2006.09.001
Stevens Thomas, Lu H, Thomas DSG, Armitage SJ. 2008. Optical dating of abrupt shifts in the late Pleistocene East Asian monsoon. *Geology* **36**(5): 415. https://doi.org/10.1130/G24524A.1
Stevens T, Carter A, Watson TP, Vermeesch P, Andò S, Bird AF, Lu H, Garzanti E, Cottam MA, Sevastjanova I. 2013. Genetic linkage between the Yellow River, the Mu Us desert and the Chinese Loess Plateau. *Quaternary Science Reviews* **78**: 355–368. https://doi.org/10.1016/j.quascirev.2012.11.032
Stevens Thomas, Buylaert J-P, Lu H, Thiel C, Murray A, Frechen M, Yi S, Zeng L. 2016. Mass accumulation rate and monsoon records from

Xifeng, Chinese Loess Plateau, based on a luminescence age model: Monsoon records from Chinese Loess Plateau. *Journal of Quaternary Science* **31**(4): 391–405. https://doi.org/10.1002/jqs.2848

Stevens T, Buylaert J-P, Thiel C, Újvári G, Yi S, Murray AS, Lu H. 2018. Ice-volume-forced erosion of the Chinese Loess Plateau global Quaternary stratotype site. *Nature Communications* **9**(1): 983. https://doi.org/10.1038/s41467-018-03329-2

Stevens T. 2019. Applications in loessic environments. In *Handbook of Luminescence Dating*, Bateman M, and Bailiff I (Ed.). Caithness, Whittles Publishing, 153–190.

Stoops G. 2003. *Guidelines for Analysis and Description of Soil and Regolith Thin Sections*. Soil Science Society of America: Madison, Wisconsin; 184.

Sun J. 2002. Source Regions and Formation of the Loess Sediments on the High Mountain Regions of Northwestern China. *Quaternary Research* **58**(3): 341–351. https://doi.org/10.1006/qres.2002.2381

Sun J, Liu T. 2000. Stratigraphic Evidence for the Uplift of the Tibetan Plateau between ~1.1 and ~0.9 myr Ago. *Quaternary Research* **54**(3): 309–320. https://doi.org/10.1006/qres.2000.2170

Sun Y, An Z. 2005. Late Pliocene-Pleistocene changes in mass accumulation rates of eolian deposits on the central Chinese Loess Plateau. *Journal of Geophysical Research* **110**(D23): D23101. https://doi.org/10.1029/2005JD006064

Sun Y, Clemens SC, Morrill C, Lin X, Wang X, An Z. 2012. Influence of Atlantic meridional overturning circulation on the East Asian winter monsoon. *Nature Geoscience* **5**(1): 46–49. https://doi.org/10.1038/ngeo1326

Thiel C, Buylaert J-P, Murray A, Terhorst B, Hofer I, Tsukamoto S, Frechen M. 2011. Luminescence dating of the Stratzing loess profile (Austria) – Testing the potential of an elevated temperature post-IR IRSL protocol. *Quaternary International* **234**(1): 23–31. https://doi.org/10.1016/j.quaint.2010.05.018

Timar A, Vandenberghe D, Panaiotu EC, Panaiotu CG, Necula C, Cosma C, van den haute P. 2010. Optical dating of Romanian loess using fine-grained quartz. *Quaternary Geochronology* **5**(2): 143–148. https://doi.org/10.1016/j.quageo.2009.03.003

Timar-Gabor A, Buylaert J-P, Guralnik B, Trandafir-Antohi O, Constantin D, Anechitei-Deacu V, Jain M, Murray AS, Porat N, Hao Q, Wintle AG. 2017. On the importance of grain size in luminescence dating using quartz. *Radiation Measurements* **106**: 464–471. https://doi.org/10.1016/j.radmeas.2017.01.009

Újvári G, Kovács J, Varga G, Raucsik B, Marković SB. 2010. Dust flux estimates for the Last Glacial Period in East Central Europe based on terrestrial records of loess deposits: A review. *Quaternary Science Reviews* **29**(23): 3157–3166. https://doi.org/10.1016/j.quascirev.2010.07.005

Vandenberghe J. 2013. Grain size of fine-grained windblown sediment: A powerful proxy for process identification. *Earth-Science Reviews* **121**: 18–30. https://doi.org/10.1016/j.earscirev.2013.03.001

Vriend M, Prins MA, Buylaert J-P, Vandenberghe J, Lu H. 2011. Contrasting dust supply patterns across the north-western Chinese Loess Plateau during the last glacial-interglacial cycle. *Quaternary International* **240**(1): 167–180. https://doi.org/10.1016/j.quaint.2010.11.009

Wang L, Jia J, Xia D, Liu H, Gao F, Duan Y, Wang Q, Xie H, Chen F. 2019a. Climate change in arid central Asia since MIS 2 revealed from a loess sequence in Yili Basin, Xinjiang, China. *Quaternary International* **502**: 258–266. https://doi.org/10.1016/j.quaint.2018.02.032

Wang L, Jia J, Zhao H, Liu H, Duan Y, Xie H, Zhang DD, Chen F. 2019b. Optical dating of Holocene paleosol development and climate changes in the Yili Basin, arid central Asia. *The Holocene* **29**(6): 1068–1077. https://doi.org/10.1177/0959683619831432

Wyrwoll K-H, Wei J, Lin Z, Shao Y, He F. 2016. Cold surges and dust events: Establishing the link between the East Asian Winter Monsoon and the Chinese loess record. *Quaternary Science Reviews* **149**: 102–108. https://doi.org/10.1016/j.quascirev.2016.04.015

Xu Z, Stevens T, Yi S, Mason JA, Lu H. 2018. Seesaw pattern in dust accumulation on the Chinese Loess Plateau forced by late glacial shifts in the East Asian monsoon. *Geology* **46**(10): 871–874. https://doi.org/10.1130/G45105.1

Yang S, Ding Z. 2010. Drastic climatic shift at ~2.8Ma as recorded in eolian deposits of China and its implications for redefining the Pliocene-Pleistocene boundary. *Plio-Pleistocene Correlation and Global Change* **219**(1): 37–44. https://doi.org/10.1016/j.quaint.2009.10.029

Yang S, Ding Z, Li Y, Wang X, Jiang W, Huang X. 2015. Warming-induced northwestward migration of the East Asian monsoon rain belt from the Last Glacial Maximum to the mid-Holocene. *Proceedings of the National Academy of Sciences* **112**(43): 13178. https://doi.org/10.1073/pnas.1504688112

Yang H, Li G, Huang X, Wang X, Zhang Y, Jonell TN, Jin M, Chen C, Zhao W, Zhang H, Wang Z, Deng Y. 2020. Loess depositional dynamics and paleoclimatic changes in the Yili Basin, Central Asia, over the past 250 ka. *Catena* **195**: 104881. https://doi.org/10.1016/j.catena.2020.104881

Youn JH, Seong YB, Choi JH, Abdrakhmatov K, Ormukov C. 2014. Loess deposits in the northern Kyrgyz Tien Shan: Implications for the paleoclimate reconstruction during the Late Quaternary. *Catena* **117**: 81–93. https://doi.org/10.1016/j.catena.2013.09.007

